



141
976
THS

LIBRARY
Michigan State
University

This is to certify that the
dissertation entitled

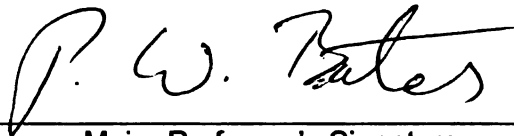
KINESIN-MICROTUBULE INTERACTIONS: TRANSPORT
AND SPINDLE FORMATION

presented by

Zhiyuan Jia

has been accepted towards fulfillment
of the requirements for the

Doctoral degree in Mathematics



Major Professor's Signature

August 27, 2009

Date

MSU is an Affirmative Action/Equal Opportunity Employer

PLACE IN RETURN BOX to remove this checkout from your record.
TO AVOID FINES return on or before date due.
MAY BE RECALLED with earlier due date if requested.

DATE DUE	DATE DUE	DATE DUE

KINESIN-MICROTUBULE INTERACTIONS: TRANSPORT AND SPINDLE
FORMATION

By

Zhiyuan Jia

A DISSERTATION

Submitted to
Michigan State University
in partial fulfillment of the requirements
for the degree of

DOCTOR OF PHILOSOPHY

Mathematics

2009

ABSTRACT

KINESIN-MICROTUBULE INTERACTIONS: TRANSPORT AND SPINDLE FORMATION

By

Zhiyuan Jia

This thesis consists of two parts. The first part concerns the detailed modeling of kinesin locomotion along microtubules. The second concerns modeling the self-organization process of kinesin and microtubules.

Kinesin-1 is composed of two identical heavy chains forming the two motor domains, called heads by biologists. The neck linker connects the head and the coiled-coil stalk. Kinesin-1 converts the chemical energy from Adenosine triphosphate (ATP) hydrolysis into locomotion along the microtubule by alternately exchanging the trailing and the leading head. Kinesin-1 takes 8 nm for each step by consuming one ATP molecule. We carried out detailed simulations for the different chemical and mechanical processes of the two heads of kinesin. Furthermore, simulations are performed with different lengths of the neck linker and the mean speed of kinesin movement is obtained. Our analysis and simulation shed light on understanding the processivity of kinesin, the estimation of the tension in neck linkers and further the role of tension in regulating the chemical states of two heads.

In the second part [36], Monte Carlo type simulations were implemented for the self-organization of microtubules interacting with molecular motors. Microtubules are treated as stiff polar rods of equal length exhibiting anisotropic diffusion in the plane. The molecular motors are implicitly introduced by specifying certain probabilistic collision rules resulting in realignment of the rods. This approximation of the complicated microtubule-motor interaction by a simple instant collision allows us to by-pass the computational bottlenecks associated with the details of the diffusion and the dynamics of motors and the reorientation of microtubules. Consequently, we

are able to perform simulations of large ensembles of microtubules and motors on a very large time scale. This simple model reproduces all important phenomenology observed in *in vitro* experiments: formation of vortices for low motor density and ray-like asters and bundles for higher motor density.

ACKNOWLEDGMENT

I am grateful for the help and guidance in those years from my mentor Professor Peter W Bates. I benefit tremendously from working with him from which I learned how to conduct scientific thinking, to extract information from experimental results, to propose an idea, and to transform it into mathematical equations. I appreciate every effort Professor Bates has made to help me meet his expectations.

I appreciate the help and encouragement from my committee members. I am grateful to the many suggestions from Professor Chichia Chiu. I enrolled and enjoyed the class of Professor Thomas Pence and I learned a lot from our discussions of the microtubule pattern modeling in spring, 2006. The enthusiasm and ambition of Professor Moxun Tang for the mathematical biology definitely influenced me doing the research in this field. The methods and skills learned from the classes of Professor Guowei Wei turned out to be important in my research.

I appreciate the help of Professor Weil for providing the support for using Latex in the writing of this thesis.

I own my parents a debt of gratitude for their constant trust in me and encouragement to move forward.

Last but not least, I thank my wife Wan and my son Will, who give me the love, the support, and the hope, which inspire me to overcome difficulties on the way.

TABLE OF CONTENTS

List of Tables	vi
List of Figures	vii
1 Introduction to Kinesin and Microtubules	1
1.1 Microtubules	1
1.2 General Results with Kinesin	2
1.3 Literature Review	6
1.3.1 Theoretical Modeling Work of Kinesin	6
1.3.2 Interactions of Kinesins and Microtubules	13
2 Regulation of Tensions of neck-linkers in Chemomechanical Processes	19
2.1 Experimental Results of Kinesin with Extended Neck-linkers	19
2.2 Bias of Kinesin Walking	22
2.3 Processivity of Kinesin Walking	25
2.4 Biochemical Reaction Cycle of Kinesin	30
2.5 Tension Estimate of the neck-linkers	32
2.6 Algorithm	37
2.7 Simulation Results	43
2.8 Discussion	58
3 Interactions between Microtubules and Molecular Motors	61
3.1 Essentials of the Model	61
3.2 Algorithm Description	66
3.3 Coarse-grained Variables	68
3.4 Pattern Characterization	68
3.5 Simulation Results	72
3.6 Conclusion	78
4 Summary and Future work	80
A Pseudo Code of the Algorithms	82
Bibliography	85

LIST OF TABLES

2.1	The reaction rate constants	31
2.2	The total lengths, persistence lengths and natural lengths of the neck-linkers.	33
2.3	The spring constants and the natural lengths of the neck-linkers . . .	36

LIST OF FIGURES

1.1	Schematic representations of microtubule. The dark monomer denotes β tubulins and the light monomer is for α tubulins.	3
1.2	Schematic representations of kinesin-1 (shown by permission from Cell Press). The two motor domains (around 5 nm) are shown in the left hand end and the two cargo binding domains are shown in the right hand end. The middle coiled-coil part is the stalk, around 70nm. . . .	3
1.3	Illustration of the kinetic diagram for a motor with $N = 3$ chemical states. The squares represent the lattice sites on the track with d , being the step size of the motor. Here we show two consecutive lattice sites labeled by ld and $(l + 1)d$. The chemical reaction cycle of a motor consists of three states denoted by 0_l , 1_l and 2_l . 0_l represents the empty state. 1_l m represent the ATP bound state and 2_l represents the ADP bound state. (shown by permission from Physica A [24].) .	10
1.4	Experiment results of the pattern formation in [62](shown by permission from Science). They used fluorescence to highlight the accumulation of the motors. The positions where there are more motors are bright.	14
2.1	Illustration of the mutants and the results of run length, speed, ATPase rate and coupling ratio. This figure is figure 1 in [95](shown by permission from Cell Press)	20
2.2	The experimental result: the histograms of stepsize of the wild type and mutant kinesins	23
2.3	Simulation results from (2.1) in graph a and from (2.3) in graph b. $c = 1/200$ is used for these graphs	26

2.4	A chemomechanical cycle of kinesin. The letters represent the nucleotide states of a kinesin catalytic core; E is for the empty state, T is for the ATP bound state, D is for the ADP bound state, DP is for the intermediate state after the ATP molecule is hydrolyzed. The dark solid oval represents head2 and the light solid oval represents head1. .	28
2.5	Illustration of the binding sites for the wild type kinesin. Three vertical stripes represent three protofilaments of the microtubule. Assume that kinesin can only bind to the sites on these three neighboring protofilaments. The oval with X inside denotes the bound head, i.e., head2 in the algorithm and the dark head in Figure 2.4. The oval represents head1 in the algorithm, the light head in Figure 2.4. The five forward binding sites for head1 are represented by squares. The number of binding sites for the mutants will increase depending on the reachable range of head1 of the mutants. Notice that the binding sites are arranged to reflect the helical structure of the microtubule.	38
2.6	Speed of the wild type, 0P-26P and 14GS mutants computed by formulas (2.24, 2.26, 2.28)	44
2.7	The speed of wild type kinesin vs ATP concentration (μM)	45
2.8	The average dwelling time of the wild type, 0P-26P and 14GS mutants	46
2.9	The average diffusion time of the wild type, 0P-26P and 14GS mutants	47
2.10	Speed of the wild type, 0P-26P and 14GS mutants	48
2.11	Coupling ratio of the wild type, 0P-26P and 14GS mutants	49
2.12	Runlength of the wild type, 0P-26P and 14GS mutants. The mean run length is shown in the insets.	50
2.13	Trajectory samples of wild type kinesin and 0P, 2P, 4P and 6P mutants.	51
2.14	Trajectory samples of wild type kinesin and 13P, 19P, 26P and 14GS mutants.	52
2.15	Stepsize histogram of the wild type and mutant kinesins.	53
2.16	The histogram of stepsize from the simulation results for the wild type, 6P, 13, 19P, 26P, and 14GS mutants. The histograms of experimental results are shown in Figure 2.15.	54

2.17	Trajectory samples of wt, 6P, 13P, 19P, 26P, and 14GS from the experimental results. These trajectories have more or less the same slope because they are obtained from different ATP concentrations. See the simulation results in Figure 2.18	55
2.18	Simulation results for the trajectories of wt, 6P, 13P, 19P, 26P, and 14GS. The same ATP concentration, 1 mM, is used in the simulation. See the experiment trajectories in Figure 2.17	56
3.1	Schematics of an alignment event (inelastic collision) between two microtubules interacting with one multi-headed molecular motor. The black dots represent the center of mass of the microtubules. (a) A multi-headed molecular motor cluster attached at the intersection point of microtubules moves from the negative (−) towards the positive (+) end of the microtubules. (b) After the interaction, the orientational angles $\varphi_{1,2}$ and the corresponding positions of the midpoints $\mathbf{R}_{1,2}$ become aligned.	63
3.2	Snapshots illustrating the patterns developing in a configuration of 6,000 rods for different motor densities, i.e., different values of P_0 . Arrows represent microtubules, circles depict the cores of vortices or asters. (a) vortices, $t = 620$, $\beta = 1.0$, $P_0 = 0.08$ (low motor density); (b) asters, $t = 602$, $\beta = 0.95$, $P_0 = 0.10$, (high motor density); (c) bundles, $t = 400$, $\beta = 1.0$, $P_0 = 0.15$. See also [100] for movies # 1,2 illustrating the self-organization process.	69
3.3	Coarse-grained images corresponding to parameters of Fig.3.2 for vortices (a) and asters (b). Arrows represent the orientation field τ . The color (grey levels) shows the density ρ , red (bright) corresponds to the maximum of ρ , and blue (dark) to its minimum. See also [100] for movies # 3,4.	75
3.4	Averaged number of asters (squares), anti-asters (diamonds), and vortices (circles) as a function of the interaction probability P_0 for two different values of parameter β . The data for $\beta = 0.35$ is shown in dashed lines, open symbols, and for $\beta = 0.95$ is shown in dotted lines, closed symbols.	76
3.5	Phase diagram of various regimes as a function of the motor density P_0 (the horizontal axis) and the anisotropy parameter β (the vertical axis). The disordered region is blue (black) here; the vortex region is green (grey); the transition from vortex to aster happens at the yellow region (white) and red (dark grey) denotes aster regions. The dashed line denotes the boundary where the rods become bundled.	77

Chapter 1

Introduction to Kinesin and Microtubules

1.1 Microtubules

The microtubule is one of three cytoskeletons in a cell. The other two are actin and intermediate filaments. The microtubule is the most rigid among them. The cytoskeletons can form the scaffolds to support and maintain the shape of a cell. In cell movement, the structure and the distribution of the cytoskeletons will adapt to facilitate moving. Actin filaments and microtubules are also the tracks for molecular motors to move on carrying cargoes such as mRNA, neuro-transmitters, etc. Microtubules are also an indispensable part of the spindle, the machinery of cell division.

Microtubules have long rigid cylindrical structures (length tens of microns and diameter approximately 25 nm) comprising of heterogeneous tubulin dimers, each dimer consisting of an α and a β tubulin, which self-assemble, 13 protofilaments being required side-to-side to form the circular cross section (see Figure 1.1). The length of a tubulin dimer is 8 nm so a microtubule filament can be seen as a linear periodic track with periodicity 8 nm. Since the microtubule is polymerized by $\alpha\beta$

tubulin dimers, one end of it exposes β tubulin. The other end exposes α tubulin and the β tubulin end has high polymerization speed and the α end has low speed. Biologists designate the end with fast polymerization speed as the plus end and the other end the minus end.

1.2 General Results with Kinesin

There are many molecular motors in each cell conducting different tasks to maintain the functions of the cell. For instance, DNA polymerase and RNA polymerase are the motors moving along the DNA strand performing the replication and the transcription of the DNA correspondingly. In this thesis, we will focus on a particular molecular motor, kinesin [33, 79], which moves on microtubules. Kinesin can carry cargoes from one place to another within the cell and can work with other motors in the cell to facilitate the division process.

Kinesin converts chemical energy, hydrolyzed from ATP (Adenosine triphosphate) molecules, into mechanical movements in a walking process. Most members of the kinesin family walk toward the plus end of microtubules. Only one subfamily, kinesin-14, NCD, a representative member, walks toward the minus end [64]. In the first part of this dissertation we will conduct detailed modeling of the walking of conventional kinesin, also called kinesin-1, since it has been investigated most extensively by biologists. From now on, for brevity, we always use kinesin for kinesin-1. In the second part of the dissertation, we will model the interactions between kinesins and microtubules and reproduce the self-organization process of the microtubules into different patterns.

Kinesin is composed of two identical heavy chains, each of them includes a N-terminal motor domain, in which there is an ATP binding site. The neck-linker is the segment in each heavy chain connecting the head to the coiled-coil stalk (See

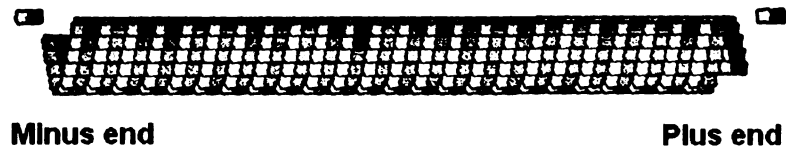


Figure 1.1: Schematic representations of microtubule. The dark monomer denotes β tubulins and the light monomer is for α tubulins.

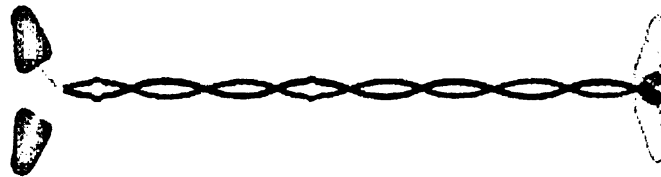


Figure 1.2: Schematic representations of kinesin-1 (shown by permission from Cell Press). The two motor domains (around 5 nm) are shown in the left hand end and the two cargo binding domains are shown in the right hand end. The middle coiled-coil part is the stalk, around 70nm.

Figure 1.2). Growing from the other end of the coiled-coil stalk are the two light chains (arms), which can hold cargoes (e.g. mRNAs, protein complexes). Kinesin has different microtubule binding affinities when in different nucleotide states [89], that is, when its core contains either ATP, ADP, or is empty. Kinesin has the weakest binding strength when its catalytic core contains an Adenosine diphosphate (ADP) molecule. Kinesin binds to the microtubule strongest when in the ATP bound state. The microtubule binding affinity has an intermediate strength when it is in the nucleotide free state. Kinesin has been demonstrated to walk in a hand-over-hand manner [93, 8]. The two heads of the kinesin molecule alternately bind to and unbind from the microtubule with mechanisms that provide a bias to the Brownian motion expected. The center of mass of the kinesin moves 8 nm with each step, which is exactly the length of one $\alpha\beta$ tubulin dimer. Kinesin consumes one ATP molecule each step, meaning that kinesin tightly couples a chemical reaction to a mechanical movement [84, 17, 34, 83]. Kinesin walks processively on a microtubule, with experimental results indicating that it can walk continuously for over 100 steps without falling off.

Kinesin primarily walks toward the plus end of microtubule while it will walk backward more likely when a backward-pointing force of sufficient strength is applied to it. The stall force of kinesin, around 7 piconewton (pN), is the force where kinesin has the same probability to walk either forward or backward. Thus, at the stall force, the walking speed of kinesin is zero [13].

Currently, a consensus model regarding the walking of kinesin is proposed as follows [94, 11].

1. Starting from a two head bound state where the leading head is in the nucleotide free state and the trailing head has an ADP molecule bound in its catalytic core.
2. The trailing head detaches from the microtubule and begins a tethered diffusion process. An ATP molecule comes and binds with the leading head. This ATP

binding releases energy which triggers part of the neck-linker to bind toward the front of the leading head and become immobile (called zipping). The length of the docked part of the neck-linker is about 2 nm at most. This neck-linker docking [74], together with another mechanism, arising from the asymmetric steric effect [87], such as the shape of the head and the shape of the binding site, provides a bias for the trailing head to step toward the next binding site in the positive direction of the microtubule.

3. After the tethered trailing head reaches the next binding site, it binds to the microtubule tightly with the release of ADP. This tight binding induces a strain on the new leading head to prevent the binding of an ATP molecule. Then the ATP molecule in the trailing head hydrolyzes and a P_i is released. The hydrolysis energy facilitates the unbinding of the trailing head and the intramolecular strain caused by the binding of the leading head now is also released.
4. Now the leading head is in the empty state and is ready for the binding of an ATP molecule and the trailing head is in the weak binding state with ADP in its catalytic core. This completes one chemomechanical cycle of kinesin.

In step 2 of the above process, when the trailing head detaches from the microtubule, it will diffuse subject to the physical restriction of the total length of the neck-linkers and their flexibility. In this process, it can temporary bind to a rearward binding site but this binding is weak because the trailing head is still in the ADP bound state. There are two hypotheses for the trailing head not to release the ADP when it binds backward. Its β sheet is in an upright position that inhibits the release of the ADP molecule [45]. There may exist a specific configuration between the neck-linker and the head which plays a role in preventing the release of ADP when the neck-linker is pointing forward. Therefore the trailing head will eventually unbind again, diffuse and bind to a forward binding site while ADP remains bound to it.

After the neck-linker of the bound head is zipped, the tethered head cannot reach the rearward binding sites because of the shortened neck-linker.

With regard to the bias of kinesin movement, there are basically two models for it. One argues that ATP-dependent neck-linker docking throws the tethered head forward to the next binding site. The other more emphasizes the diffusive search of the tethered head for the next binding site with more likelihood of binding forward because the neck-linker is zipped towards the front of the bound head. Both of them conjecture that the forward binding of the tethered head, accompanied by the release of ADP, is strong so that it completes a step. Certainly these two models are not mutually exclusive and they actually work together in our model.

Steric asymmetry is another source of bias [87]. The evidence of steric bias can be seen in a series of experiments where the kinesin can walk toward either the plus or the minus end depending on the applied external force when there is no ATP at all, only ADP or AMPPNP (Adenylyl-imidodiphosphate, a nonhydrolyzable ATP analog). The X-ray crystallography of a kinesin-microtubule complex suggests the different binding conformations of leading and trailing heads when kinesin is in a two-head-bound state [45, 80]. The leading head is in a tilted configuration and the trailing head is in an upright configuration. The backward binding of the trailing head favors an upright conformation due to the forward tension. It is believed that the tilted configuration is required for the release of ADP.

1.3 Literature Review

1.3.1 Theoretical Modeling Work of Kinesin

Biological experiments have stimulated many theoretical works to elucidate the different aspects of the walking mechanism of kinesin, such as the bias and the processivity of the movement. Basically there are two different approaches to the theoretical

modeling. One is the continuum ratchet method, using a damped Langevin equation [32, 41] or a set of coupled Fokker-Planck equations [32, 41] to describe the movement of kinesin by assuming that kinesin is subject to different potentials when it is in different chemical states. The potentials are chosen to be asymmetric over an 8 nm periodic interval to generate the biased movement of kinesin. The transitions among the different potentials depend on the chemical states, the concentration of ATP(ADP), and the external force and can be described by the transition rates, which are tuned to coordinate the potentials. In this method, it is challenging to derive realistic potential functions, (see for instance [38, 40, 42, 44, 59, 57, 65, 68, 73]).

In the following, we examine an example from [38], where the authors used the Langevin model to discuss the speed dependence on ATP concentration, the stall force, the trajectory, and the processivity of kinesin. The plus end of the microtubule is taken to be the positive direction of the x axis and the coordinates of the tethered head of the kinesin are (x, y) , where y represents the one-dimensional displacement of the head perpendicular to the microtubule. The Langevin system reads as

$$\begin{aligned}\gamma\dot{x} &= -\frac{\partial H_{ratchet}}{\partial x} - \frac{\partial H_{bistable}}{\partial x} + F_{ext}^x + \sqrt{2K_B T \gamma} \frac{dW_x}{dt}, \\ \gamma\dot{y} &= -\frac{\partial H_{ratchet}}{\partial y} - \frac{\partial H_{bistable}}{\partial y} + F_{ext}^y + \sqrt{2K_B T \gamma} \frac{dW_y}{dt},\end{aligned}\tag{1.1}$$

where γ is the drag coefficient, $\frac{dW}{dt}$ is white noise, $H_{ratchet}$ is a periodic function in x , i.e., $H_{ratchet}(x + 2L, y, t) = H_{ratchet}(x, y, t)$, and $L = 8\text{nm}$ is the period of the microtubule. Specifically, $H_{ratchet}$ is given by

$$H_{ratchet}(x, y, t) = S(t)C[Hx(x)Hy(y)] - \alpha y,\tag{1.2}$$

where $C = 0.8\text{ eV}$ and $\alpha = 0.044\text{ eV}$ are constants, $S(t)$ is a switch function

$$S(t) = \begin{cases} 1, & \text{on state} \\ 0.1, & \text{off state} \end{cases}$$

which is supposed to produce a flashing ratchet. The authors select a number $p_{flashing}$ between 0 and 1 in advance for the simulation, representing the probability of random arrivals of the ATP molecules. The motor is in the on state as a simulation begins. A uniformly distributed random variable ζ is generated in each simulation step to compare it with $p_{flashing}$. If $p_{flashing} > \zeta$, then the state of the motor is switched off. Otherwise, it will stay in the on state.

The function H_x is given by

$$H_x(x) = a_0 + \sum_{m=1}^5 a_m \cos\left(\frac{2m\pi x}{2L}\right) + \sum_{m=1}^5 b_m \sin\left(\frac{2m\pi x}{2L}\right), \quad (1.3)$$

which is the truncated Fourier expansion of the following asymmetric potential function

$$U(x) = \begin{cases} \frac{10}{9} \left(\frac{x}{2L} - \left[\frac{x}{2L} \right] \right), & \frac{x}{2L} - \left[\frac{x}{2L} \right] < 0.9, \\ 10 \left(\frac{x}{2L} - \left[\frac{x}{2L} \right] \right) - 10, & \frac{x}{2L} - \left[\frac{x}{2L} \right] > 0.9, \end{cases}$$

where $\left[\frac{x}{2L} \right]$ is the integer part of the ratio.

The function H_y is given by

$$H_y(y) = \exp\left(-\frac{2(y - y_0)}{\beta}\right) - 2\exp\left(\frac{y - y_0}{\beta}\right), \quad (1.4)$$

where $\beta = 5L = 40 \text{ nm}$ and $y_0 = L = 8 \text{ nm}$ were used. The term H_y is supposed to model the van der Waals interaction between the head of kinesin and the microtubule.

The function $H_{bistable}$ is given by

$$H_{bistable}(\Delta r) = C_1 \left[1 + \left(\frac{\Delta r}{\ell} \right)^4 - 2 \left(\frac{\Delta r}{\ell} \right)^2 \right],$$

where Δr is the distance between the two heads, $C_1 = 5.4eV$ represents the coupling strength of the two heads, $\ell = 0.75L$, and 2ℓ is the distance between the two minima of the potential.

By solving the above 2D Langevin equation (1.1), the authors produced trajectories of the two heads of kinesin in a hand-over-hand walking process. They also tested the relation between the speed and the external force and found the value of the stall force to be 6.4 pN, which is in close to the experimental result, around 7 pN. The authors also tested the processivity of the model and claimed that the motor described by their model does have processivity. The potentials and parameter values used in this model have not been justified, however. For instance, they pointed out that the last term αy in (1.2) is critical to have the processivity of the motor but they could not give a physical or chemical reason for the use of this term.

From this example we can see that, to have a realistic continuum ratchet model, it is critical to construct potential functions which can reflect the structure of the kinesin heads in different chemical states and the interactions with the protofilaments of microtubules. For this we need further information about the structures and interactions.

The second approach uses discrete chemical kinetic networks to model the free energy transduction in the walking process [70, 23, 24, 71, 25, 52, 54, 88]. An example from [23, 25] can help illustrate the basic idea of the stochastic discrete kinetic method.

A schematic illustration of the walking of a motor on a linear periodic track is shown in Figure 1.3. Corresponding to Figure 1.3, the sequential kinetic equation can be described as follows.

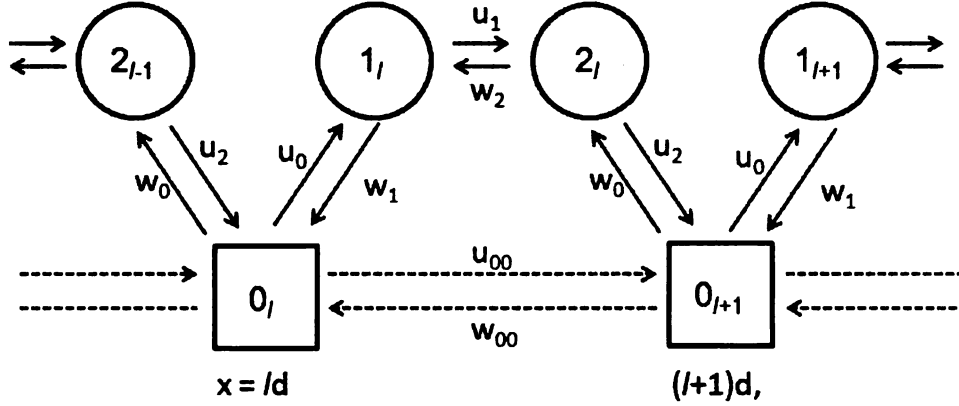


Figure 1.3: Illustration of the kinetic diagram for a motor with $N = 3$ chemical states. The squares represent the lattice sites on the track with d , being the step size of the motor. Here we show two consecutive lattice sites labeled by ld and $(l + 1)d$. The chemical reaction cycle of a motor consists of three states denoted by 0_l , 1_l and 2_l . 0_l represents the empty state. 1_l m represent the ATP bound state and 2_l represents the ADP bound state. (shown by permission from Physica A [24].)

$$0_l \xrightleftharpoons[w_1]{u_0} 1_l \xrightleftharpoons[w_2]{u_1} 2_l \cdots \xrightleftharpoons[w_{N-1}]{u_{N-2}} (N-1)_l \xrightleftharpoons[w_0]{u_{N-1}} 0_{l+1}, \quad (1.5)$$

where the lattice sites on the track are labeled by l ($= 0, \pm 1, \pm 2, \dots$) and the chemical states are denoted by $j = 0$ for the free state, i.e., no ATP bound state, and $j = 1, 2, \dots, N - 1$ for the other various bound states, where N is the number of the total chemical states. Thus j_l represents the situation where the motor lands at the l^{th} lattice site and is in the j^{th} chemical state. The distance between two lattice sites, l and $l + 1$, equals the step size d as is shown in Figure 1.3. The reaction rates u_j and w_j are independent of the lattice position. Let $P_j(l, t)$ be the probability of finding the motor at the site l with the state j at time t . The time evolution equation for $P_j(l, t)$ is

$$\frac{\partial}{\partial t} P_j(l, t) = u_{j-1} P_{j-1}(l, t) + w_{j+1} P_{j+1}(l, t) - [u_j + w_j] P_j(l, t), \quad (1.6)$$

for $j = 0, 1, \dots, N-1$ with periodic conditions

$$\begin{aligned} P_{-1}(l, t) &= P_{N-1}(l-1, t), \quad P_N(l, t) = P_0(l+1, t), \\ u_{-1} &= u_{N-1} \text{ and } w_N = w_0. \end{aligned} \quad (1.7)$$

According to [21], the above equation can be solved explicitly to obtain the drift velocity in terms of the reaction rates,

$$V = \frac{d}{R_N} \left(1 - \prod_{j=0}^{N-1} \frac{w_j}{u_j} \right) \quad (1.8)$$

while

$$R_N = \sum_{j=0}^{N-1} r_j, \quad r_j = \frac{1}{u_j} \left(1 + \sum_{k=1}^{N-1} \prod_{i=1}^k \frac{w_{j+i}}{u_{j+i}} \right) \quad (1.9)$$

The diffusion constant D can be expressed as

$$D = \left(\frac{V S_N + U_N d}{R_N^2} - \frac{1}{2} (N+2) V \right) \frac{d}{N} \quad (1.10)$$

with

$$S_N = \sum_{j=0}^{N-1} s_j \sum_{k=0}^{N-1} (k+1) r_{k+j+1}, \quad U_N = \sum_{j=0}^{N-1} u_j r_j s_j, \quad (1.11)$$

while the supplementary coefficients are

$$s_j = \frac{1}{u_j} \left(1 + \sum_{k=1}^{N-1} \prod_{i=1}^k \frac{w_{j+1-i}}{u_{j-i}} \right). \quad (1.12)$$

Among those chemical steps, if one or multiple steps are assumed to be load dependent from the experimental observation, then one can derive the relation between velocity and the external load.

The above example gives the basic idea of stochastic reaction network method where a two-headed motor is simplified as one head without considering the coordination between the two heads. In [54], the authors considered the discrete reaction network with two heads and produced the velocity-force relation. There are more articles concerning the ratchet continuum method and the stochastic chemical reaction network method cited in [47].

A great deal of mathematical analysis has been inspired by attempts to provide rigorous results for the Brownian ratchet model of molecular motors, see [9, 12, 15, 16, 46, 66, 67] and the reference in these papers. Those mathematical analyses were done for continuum ratchet models. For example, A Fokker-Planck equation was considered in [15]. Assume the motor moves along a linear track and x denotes the position of the motor. Let $\rho = (\rho_1, \rho_2)$ be the probability densities of the motor at different states, say $i = 1, 2$, representing two states here. Assume that the two states are subject to different potentials. For instance, the state 1 and 2 might correspond to the zipped and unzipped state of the neck-linker. The time evolution of ρ is given by the following coupled Fokker-Planck equation.

$$\begin{cases} \frac{\partial \rho_1}{\partial t} = \frac{\partial}{\partial x} \left(\sigma \frac{\partial \rho_1}{\partial x} + \varphi'_1 \rho_1 \right) - \nu_1 \rho_1 + \nu_2 \rho_2 \\ \frac{\partial \rho_2}{\partial t} = \frac{\partial}{\partial x} \left(\sigma \frac{\partial \rho_2}{\partial x} + \varphi'_2 \rho_2 \right) + \nu_1 \rho_1 - \nu_2 \rho_2 \end{cases} \quad \text{in } \Omega, \quad t > 0 \quad (1.13)$$

with the boundary conditions,

$$\begin{cases} \sigma \frac{\partial \rho_1}{\partial x} + \varphi'_1 \rho_1 = 0 \\ \sigma \frac{\partial \rho_2}{\partial x} + \varphi'_2 \rho_2 = 0 \end{cases} \quad \text{on } \partial\Omega, \quad t > 0 \quad (1.14)$$

and

$$\begin{cases} \rho_i(x, 0) = \rho_i^0 \geq 0, \\ \int_{\Omega} (\rho_1 + \rho_2) dx = 1 \end{cases} \quad \text{in } \Omega, \quad i = 1, 2 \quad (1.15)$$

where $\Omega = (0, 1)$.

In [15], the authors proved that the stationary distribution of the probability density described by equations (1.13, 1.14, 1.15) decays exponentially.

To the best of our knowledge, there is no detailed simulation of the walking process of kinesin that faithfully follows the experimentally established biochemical and mechanical processes. In this thesis, we develop algorithms to model this chemo-mechanical process and apply the algorithm to elucidate some fundamental issues surrounding the walking of kinesin, such as the bias and the processivity. Inspired by [95], we modeled neck-linkers as entropic springs, discussed the tension estimate of the neck-linkers, and furthermore clarified the role of tensions of the neck-linkers of kinesin.

1.3.2 Interactions of Kinesins and Microtubules

Organization of complex networks of long biofilaments such as microtubules and actin filaments in the course of cellular processes and division is one of the primary functions of molecular motors [32]. A number of *in vitro* experiments were performed [86, 90, 62, 81, 35, 63] to study the interaction of molecular motors and microtubules energized by the hydrolysis of ATP in isolation from other biophysical processes simultaneously

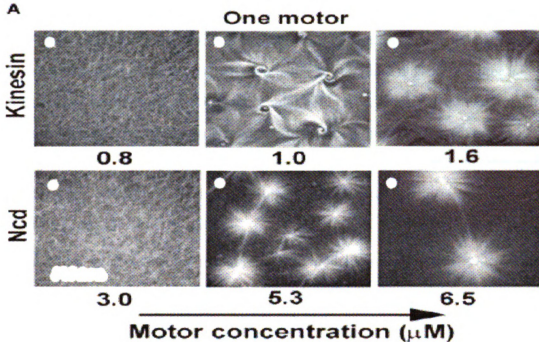


Figure 1.4: Experiment results of the pattern formation in [62](shown by permission from Science). They used fluorescence to highlight the accumulation of the motors. The positions where there are more motors are bright.

occurring *in vivo*.

In particular, the experiments in [62] used microtubules and kinesin as a model system to investigate the self-assemble process of the spindle formation. Indeed, in the cells of some organisms, for instance, plant cells, the randomly distributed microtubules are self-organized into the spindles via the interactions with the molecular motors kinesin and dynein (see [37] and the reference therein). The experiments [62] clearly demonstrated that at large enough concentration of molecular motors and microtubules, the latter organize into ray-like *asters* and rotating *vortices* depending on the type and concentration of molecular motors. These experiments spurred numerous theoretical studies addressing various aspects of self-organization of active filaments systems [51, 61, 55, 14, 19, 50, 2, 3, 92, 49, 96].

The experiments [62, 81, 35, 63] suggested the following qualitative picture of

motor-filament interaction. After a molecular motor has bound to a microtubule at a random position, it marches along it in a definite direction until it unbinds without appreciable displacement of microtubules (since the size of a molecular motor is small in comparison with that of the microtubule). However, if a molecular motor binds to *two* microtubules (some molecular motors (e.g., kinesin) form clusters with at least two binding sites), it exerts significant torques and forces, and can change the positions and orientations of the microtubules significantly, leading eventually to the onset of large-scale ordered patterns.

In [51], a set of field equations were used to model the pattern formation observed in the experiment [62, 81]. In a 2D square domain, let \vec{U} be the local orientation of microtubules and m be the concentration of the motors. The following equation is introduced in [51] to describe the evolution of the orientation of microtubules and the concentration of motors with respect to time.

$$\begin{cases} \frac{\partial m}{\partial t} = \nabla^2 m - \vec{\nabla} \cdot (m \vec{U}) \\ \frac{\partial \vec{U}}{\partial t} = C \vec{U} (1 - |\vec{U}|^2) + \vec{\nabla} \cdot (m \vec{\nabla} \vec{U}), \end{cases} \quad (1.16)$$

which is subject to the reflecting boundary conditions $\vec{U}|_{boundary} = -\hat{n}$, where \hat{n} is the normal outward vector at the boundaries. Their simulation results shown the formation of the aster and the vortex patterns. Typically there are both aster and vortex patterns at low motor concentration and the vortex becomes dominant at the high motor concentration contrary to experimental evidence. The author failed to produce the transition from vortex to aster dominance when the motor concentration increases.

Following basically the same idea, the authors in [78, 60] divided the motor population into two fractions, the free diffusion motors and the microtubule-bound motors. The concentration of the free motors fluctuates due to the binding of the free motors

and the unbinding of the microtubule-bound motors. So the first equation in (1.16) was replaced by two equations to describe the evolution of the free motors and the bound motors.

$$\begin{cases} \frac{\partial m_f}{\partial t} = D\nabla^2 m_f - \gamma_{f \rightarrow b} m_f + \gamma_{b \rightarrow f} m_b \\ \frac{\partial m_b}{\partial t} = -\nabla \cdot (m_b \vec{U}) + \gamma_{f \rightarrow b} m_f - \gamma_{b \rightarrow f} m_b \\ \frac{\partial \vec{U}}{\partial t} = \vec{U}(1 - |\vec{U}|^2) + m_b \nabla^2 \vec{U} + \epsilon \vec{\nabla} m_b \cdot \vec{\nabla} \vec{U} + \varsigma \nabla^2 \vec{U} + \xi \vec{\nabla} m_b, \end{cases} \quad (1.17)$$

where $\gamma_{b \rightarrow f}$ is the transition rate for the motor to change from the rod bound state to the free state, vice versa for $\gamma_{f \rightarrow b}$. C , ϵ , ς and ξ are parameters. Essentially, the author obtained similar results to those in [51] and unfortunately also could not produce the transition from vortex to aster patterns as the motor's concentration increased. In their simulation results, it seems what pattern will emerge relates to the boundary conditions used. When all the other parameter values are the same, aster patterns are more likely to appear with the reflecting boundary conditions and vortex patterns are more likely to be seen in the parallel boundary conditions, meaning that the orientation of the microtubules are perpendicular to the normal outward direction of the boundaries.

Small-scale molecular dynamics simulations were performed to elucidate the nature of self-organization [62, 81]. In these simulations the microtubules were modeled by semi-flexible rods diffusing in viscous fluids. Molecular motors were correspondingly modeled by short stiff linear springs with a large diffusion coefficient. Once the motor diffuses to within a certain small distance from the intersection point of two microtubules, it attaches to them with a certain probability p_{on} and marches along with velocity v . The action of the motor is to exert forces and torques on the microtubules, resulting in their mutual displacement and realignment. Then the

motor detaches with a probability p_{off} . To model the dwelling effects of the motors on the end-points of microtubules, observed for some types of molecular motors, an additional probability p_{end} to leave the end-point was assigned. The corresponding typical dwelling time t_{end} is of the order $1/p_{end}$. The simulations in [62, 81] indeed reproduced certain features of the observed phenomenology, such as the stability of patterns and transitions between vortices and asters. However, in this approach many fundamentally different time scales had to be simultaneously resolved computationally (e.g., fast diffusion of the motors and very slow pattern formation). As a result, the method is very CPU-intensive, and only a small number of microtubules were studied numerically, leaving many important questions, such as the nature of the transition and structure of the phase diagram, unanswered.

In Refs. [2, 3] a continuum probabilistic model of alignment of microtubules mediated by molecular motors was developed. The theory was formulated in terms of a stochastic master equation governing the evolution of the probability density of microtubules with a given orientation at a given location. The theory is based on a number of simple assumptions on the interaction rules between microtubules and molecular motors. In particular, only binary *instant* interactions of microtubules called *inelastic collisions* are considered. These are mediated by molecular motors in a two-dimensional microtubule-motor mixture of constant motor density. The motors are implicitly introduced into the model by specifying the probability of interaction of intersecting microtubules. Despite all the above simplifications of the biological process of self-organization of the cytoskeleton, the model reproduced, on a qualitative level, key experimental observations, such as the onset of an oriented (polar) phase above a critical density of motors, formation of asters for large density of motors and vortices for lower density, direct transition towards asters from the isotropic state for large dwelling times of the motors at the end of microtubules, and a density instability and the onset of bundle formation at very high motor density.

However, due to significant complexity of the derived stochastic master equation governing the evolution of the probability density of microtubules, the analysis in Refs. [2, 3] was carried out in a relatively narrow range of parameters, namely, in the vicinity of the orientational instability, which allowed rigorous reduction of the stochastic master equation to a set of much simpler amplitude or Ginzburg-Landau type equations for the local coarse-grained density and orientation of microtubules. This approach yields some insights into the self-organization process, but, it obviously has its own limitations.

We perform Monte Carlo type simulation studies of self-organization of microtubules interacting with molecular motors. Instead of modeling the self-organization process in all details as was done in Refs. [62, 81], we use simplified interaction rules suggested in the works [2, 3]. This simplification allows the elimination of fast time scales associated with the diffusion and motion of the motors. Consequently, one may focus on relevant time and length scales associated with large-scale pattern formation and evolution. We studied very large ensembles of microtubules and addressed questions related to the structure of the corresponding phase diagram and the transitions between various patterns. In agreement with the early experiments, we were able to reproduce aster-like structures for a high motor density and vortices for a lower density, as well as transitions to bundles. Our approach provides direct access to the dynamics of the stochastic master equation and obtains insights far beyond the amplitude equations approach. Moreover, our method provides an efficient and fast tool for simulation of complex biological process of cytoskeleton self-organization and can be possibly extended to rather different systems, such as anisotropic granular media and systems of self-propelled particles.

Chapter 2

Regulation of Tensions of neck-linkers in Chemomechanical Processes

2.1 Experimental Results of Kinesin with Extended Neck-linkers

In order for kinesin to walk over 100 steps without falling off the microtubule, there must be at least one head bound to the microtubule at all times in the walking process. So there must be a mechanism for those two heads to prevent both of them being in the ADP bound state when both are attached to the microtubules. In other words, there should be mechanisms for them to keep their chemical states out of phase. The tension of the neck-linkers is such a candidate in the regulation of the chemical states of the two heads [31, 77].

To test how the tensions in the neck-linkers help coordinate the chemical states of the two heads, Amet Yildiz et al [95] did an experiment in which they inserted

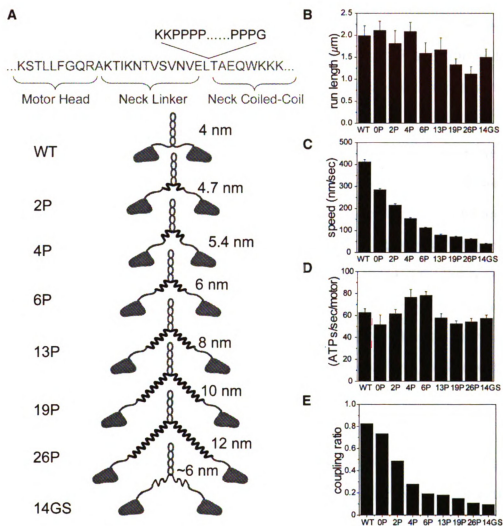


Figure 2.1: Illustration of the mutants and the results of run length, speed, ATPase rate and coupling ratio. This figure is figure 1 in [95](shown by permission from Cell Press)

different materials with different lengths into the native neck-linker. As is shown in Figure 2.1, they inserted three amino acids, represented by K(lysine)KG(glycine) in part A in Figure 2.1, at the junction of the neck-linker and the coiled-coil stalk so that the joint between the two neck-linker parts is more flexible. This mutant is labeled 0P. From the mutant 0P, they inserted polyproline (P) helices with different lengths at the position between KK and G to form the mutants 2P, 4P, 6P, 13P, 19P and 26P. Finally 14GS is the mutant formed by inserting glycine-serine (GS) repeats instead of polyproline.

Their experiment results shown that all of the mutants can still walk over 100 steps and have more or less the same run length as the wild type. However, the speed of these mutants decreases as the mutants' neck-linker becomes longer and the inserted material becomes soft. The measured ATPase rates of the mutants are the same as the wild type but much more futile cycles (where ATP is used but no step is taken) were found in the mutants. The coupling ratio of ATP, defined as the quotient of the number of steps over the number of hydrolyzed ATP molecules, decreases as the similar tendency as the speed. The coupling ratio for the wild type is about 80% but the 14GS has a ratio of only 10%.

The motility of kinesin is tested at different nucleotide conditions. If there is no ATP at all, under external forces, kinesin can walk toward either the plus or the minus end of the microtubules depending on the direction and the magnitude of the external forces. A force of 3 pN (6 pN) is required for the motor to walk toward the plus (minus) end. In this situation, there is no neck-linker docking at all and the direction of the movement is decided by the direction of the external force. The authors also tested the motor with only ADP or AMPPNP (Adenylyl-imidodiphosphate, a nonhydrolyzable ATP analog) present and found that the amplitude of the external forces for the motor to walk toward the plus end is 1 pN in ADP solution and 9 pN in AMPPNP solution. A force of 2 pN in ADP solution and 12 pN in AMPPNP solution are

required for the motor to walk toward the minus end. Therefore, the amplitude of the external forces for the kinesin to walk toward the plus end is different in the different nucleotide solutions, 1 pN in ADP solution, 3 pN in no nucleotide condition, and 9 pN in AMPPNP solution. This evidence verifies the dependence of binding affinities on the nucleotide states. On the other hand, the amplitude of the external forces for the kinesin to walk toward the minus end is also different in the different nucleotide solutions, 2 pN in ADP solution, 6 pN in no nucleotide condition, and 12 pN in AMPPNP solution. These differences in the amplitude of the external forces applied to the kinesin for the plus end walking and the minus end walking at the same nucleotide condition clearly indicate that there exists asymmetric steric binding affinities for kinesin, in addition to the binding affinities on the nucleotide states

The step size histogram of the mutants indicates that kinesin still continues to walk forward with the extended neck-linkers. There is only about 5% more backward steps for mutants compared with the wild type. With the long neck-linker and soft GS inserted, 14GS has much more lateral binding, meaning that the motor binds to the sites on the protofilaments adjacent to the one where the bound head is on, (see Figure 2.15).

2.2 Bias of Kinesin Walking

What is the origin of directional bias in the movement of kinesin along a microtubule? Rice et al. [74, 75, 76] proposed a mechanism called the neck-linker docking to explain the unidirectional stepping of kinesin. Actually neck-linker docking alone cannot explain the results in Yildiz paper [95].

Assume that kinesin walks on a protofilament of the microtubule. Its bound head is at the origin and the other head is in the tethered state. After the neck-linker is docked toward the plus end of the microtubule, the root of the free neck-linker is

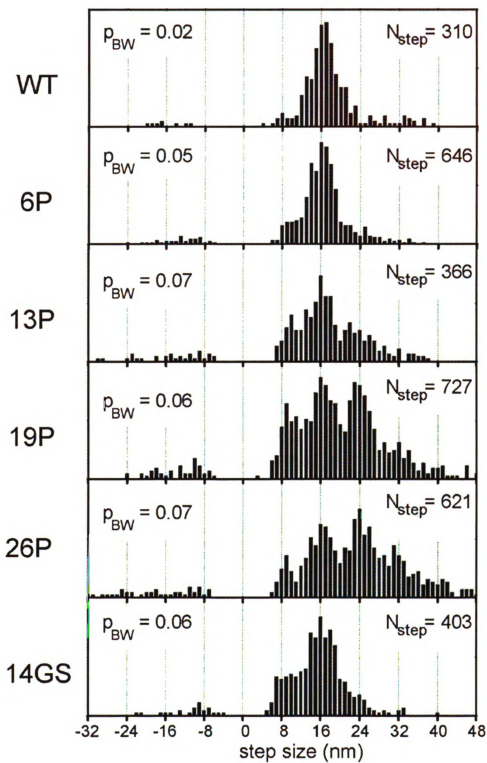


Figure 2.2: The experimental result: the histograms of stepsize of the wild type and mutant kinesins

located at $x = 2 \text{ nm}$. Assume the length of neck-linkers is long enough so that the tethered head can reach the forward binding sites $x = 8$ and $x = 16$ and the backward binding site $x = -8$ and $x = -16$. The distance from the root of neck-linker in the bound head to those four position is $d_1 = 6$, $d_2 = 10$, $d_3 = 14$ and $d_4 = 16$. The possibility for the tethered head to reach those sites decreases with respect to the distance and can be modeled as $e^{-cd_i^2}$, $i = 1, 2, 3, 4$, where c is the parameter to adjust the probabilities. After the normalization, we obtain the probability for the tethered head to bind to one of those sites

$$P_i = \frac{e^{-cd_i^2}}{\Pi}, \quad \Pi = \sum_{i=1}^4 e^{-cd_i^2}, \quad i = 1, 2, 3, 4. \quad (2.1)$$

The probabilities for the tethered to bind to the position at $x = -32, -24, -16, -8, 0, 8, 16, 24, 32$ are $p_{-32} = P_4^2$, $p_{-24} = 2P_4P_2$, $p_{-16} = P_4^2$, $p_{-8} = 2P_4P_1$, $p_0 = 2P_3P_4 + 2P_1P_2$, $p_8 = 2P_2P_3$, $p_{16} = P_1^2$, $p_{24} = 2P_1P_4$, $p_{32} = P_1^2$. Graph a in Figure 2.3 showed these probabilities and it does not have peaks at $x = 16, 24$ no matter how we adjust the value of parameter c in the formula. Therefore there must be another mechanism to bias the kinesin walking toward the plus end of microtubules. Entropy effects were investigated in [87] and showed that there is a $6K_B T$ free energy difference per step between walking toward the plus end and toward the minus end, i.e., $E_{fw}^{free} - E_{bw}^{free} = -6K_B T$, where fw and bw denote forward and backward. According to Arrhenius transition rate theory, this difference in free energy favors a biased forward walking with

$$P_{fw} = \frac{e^6}{e^6 + 1}, \quad P_{bw} = \frac{1}{e^6 + 1}. \quad (2.2)$$

Indeed, Arrhenius transition rate theory [32] gives

$$k_{fw} = Ae^{-\frac{E_{fw}^{free} - E_{activation}^{free}}{K_B T}} \text{ and } k_{bw} = Ae^{-\frac{E_{bw}^{free} - E_{activation}^{free}}{K_B T}}.$$

Then the probability for the forward and backward reactions are

$$P_{fw} = \frac{k_{fw}}{k_{fw} + k_{bw}} \text{ and } P_{bw} = \frac{k_{bw}}{k_{fw} + k_{bw}}.$$

Simple computation gives us (2.2).

After we take into account the bias for forward walking from the entropic effect in the above formula, we arrive at the following modifications to (2.1):

$$P_{1,3} = \frac{P_{fw} e^{cd_{1,3}^2}}{\Pi}, \quad P_{2,4} = \frac{P_{bw} e^{cd_{2,4}^2}}{\Pi}, \quad \Pi = P_{fw}(e^{cd_1^2} + e^{cd_3^2}) + P_{bw}(e^{cd_2^2} + e^{cd_4^2}). \quad (2.3)$$

By using the probability from (2.3) to compute the binding probabilities for the different binding sites, we produce a similar graph to that from the experimental results, (see 2.2). Therefore this simple argument indicates that neck-linker docking and entropic bias work together to be able to generate the bias seen in the experiments.

2.3 Processivity of Kinesin Walking

For kinesin to walk along a microtubule for a few micrometers without falling off, the kinesin must coordinate the chemical states of their two heads to be out of phase so that one of the heads is always bound to the microtubule. The mutants with longer neck-linkers can walk over 100 steps as the wild type. The mutants having long and(or) soft neck-linkers have small tensions in their neck-linkers. On the other

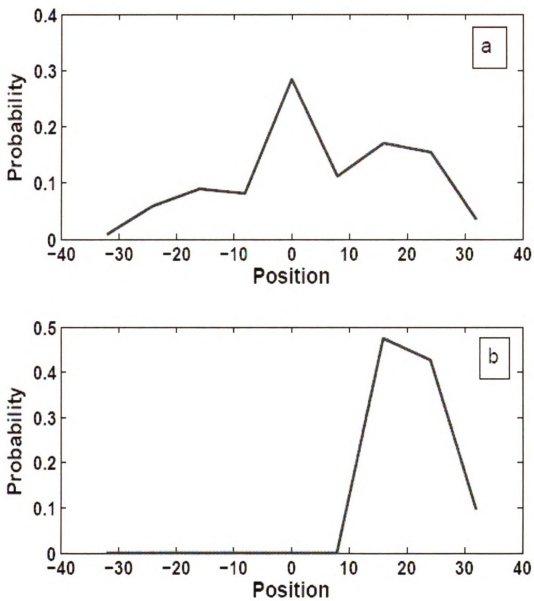


Figure 2.3: Simulation results from (2.1) in graph a and from (2.3) in graph b. $c = 1/200$ is used for these graphs

hand, if tension is the only factor to regulate the processivity, then small tensions in the mutants should lead to the loss of processivity. Therefore, the processivity of the mutants actually indicates there are other mechanisms in coordinating the chemical states.

In Figure 2.4, H1 is represented by the light head and H2 is represented by the dark head. We now examine how the chemical states of the two heads change during one step in the walking process. Starting from the moment when kinesin is in the two-head-bound state with the trailing head in the ADP bound state and the leading head in the empty state, and ending at the moment when the trailing head has taken one step forward and has become the leading head in the empty nucleotide state and the leading head has become the trailing head in ADP bound state, we can decompose this time period into several subdivisions according to the temporal order as follows:

- $T_{H1} = T_{dMT} + T_{diffusion} + T_{dADP} + T_{H1_{ATP}}$
- $T_{H2} = T_{ATP} + T_{ATPhydro} + T_{dP_i}$
- $T_{H1}^* = T_{dMT} + T_{diffusion} + T_{dADP}$

T_{dMT} is the time period between the moment when H1 acquires ADP and the moment when the head unbinds from the microtubule. $T_{diffusion}$ is the time of diffusion of H1 until it binds again to the microtubule. T_{dADP} is the time taken for H1 to release its bound ADP after H1 binds to a forward position. $T_{H1_{ATP}}$ is the time period between the moment when ADP is released until the moment when H2 releases a phosphate. T_{ATP} is the time period for H2 to bind an ATP molecule and the ATP molecule is trapped, i.e., the neck-linker is docked. $T_{ATPhydro}$ is the time elapsed from when the ATP is trapped in H2 until the ATP is hydrolyzed into ADP · P. Finally, T_{dP_i} is the time needed for H2 to release the P_i after hydrolysis. If $T_{H1}^* > T_{H2}$, then both heads will be in the ADP bound state at the same time,

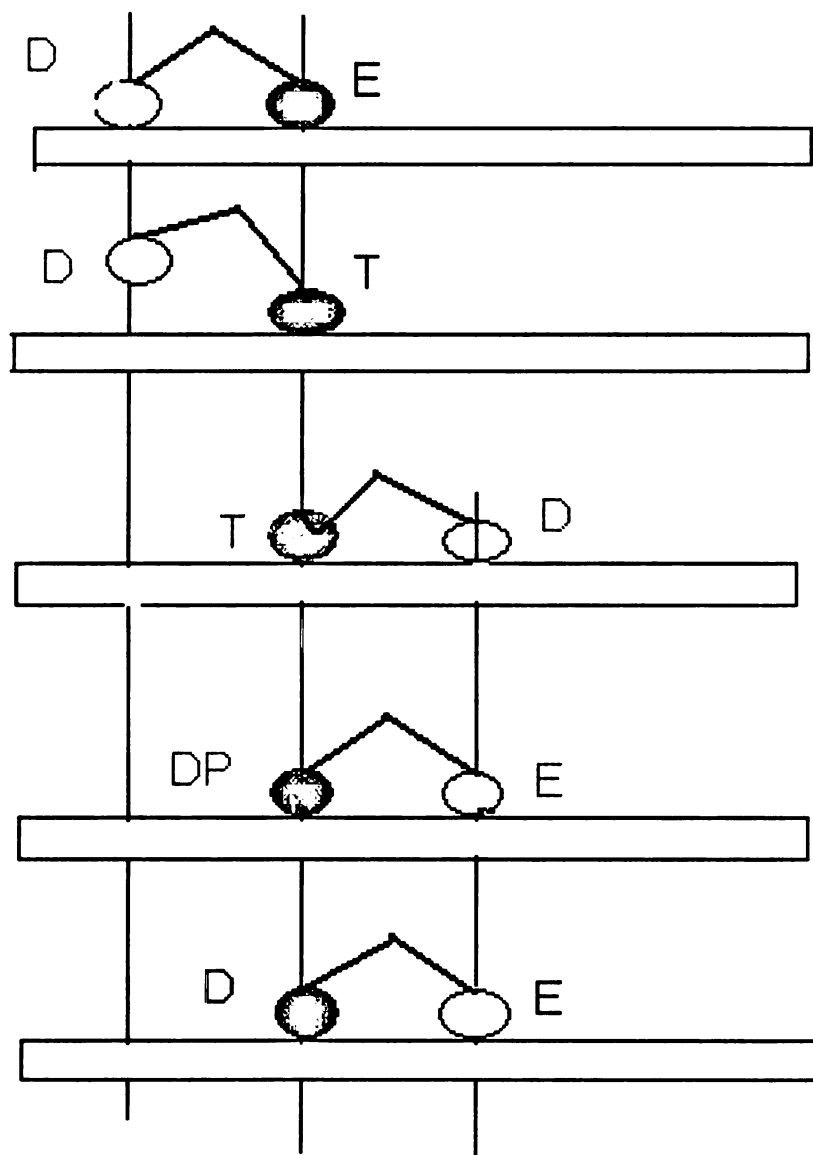


Figure 2.4: A chemomechanical cycle of kinesin. The letters represent the nucleotide states of a kinesin catalytic core; E is for the empty state, T is for the ATP bound state, D is for the ADP bound state, DP is for the intermediate state after the ATP molecule is hydrolyzed. The dark solid oval represents head2 and the light solid oval represents head1.

which has the weakest binding affinity to the microtubule and so the kinesin is likely to fall off. Therefore processivity requires $T_{H1}^* \leq T_{H2}$.

Given the inequality $T_{H1}^* \leq T_{H2}$, we next determine how T_{H1}^* and T_{H2} change with the length and the tension of the neck-linkers. There are two hypotheses concerning the tension of the neck-linkers: the front-gated-head model [30, 77] and the rear-gated-head model [31]. The front-gated-head model postulates that in the two-head-bound state with the leading head in its empty nucleotide state and the trailing head in its ADP bound state, the tension in the leading head neck-linker prevents ATP molecules binding to the leading head until the trailing head detaches from the microtubule. The rear-gated-head model [31] postulates that the tension in the trailing head neck-linker favors the dissociation of the trailing head from the microtubule. These hypotheses imply the following conclusions, respectively.

- $T_{ATP} \searrow$ as the tension \searrow
- $T_{dMT} \nearrow$ as the tension \searrow

On the other hand, if the length of the neck-linker is longer, then we know

- $T_{diffusion} \nearrow$ as the neck-linker length \nearrow

Therefore we have

- $T_{H1}^* \nearrow$ and $T_{H2} \searrow$ as the tension \searrow and the neck-linker length \nearrow

These changes with respect to the tension and the neck-linker length may break the inequality $T_{H1}^* \leq T_{H2}$ and further induce the loss of processivity. To restore the balance, we could either decrease T_{H1}^* or increase T_{H2} . To decrease T_{H1}^* , T_{dADP} ought to decrease as the tension is small. This conclusion so far has not been supported by experimental results. To increase T_{H2} , we can increase either $T_{ATPhydro}$ or T_{dP_i} or both. Under the condition of saturated ATP, the rate-limiting step in the ATP hydrolysis process turns out to be the P_i release. Therefore

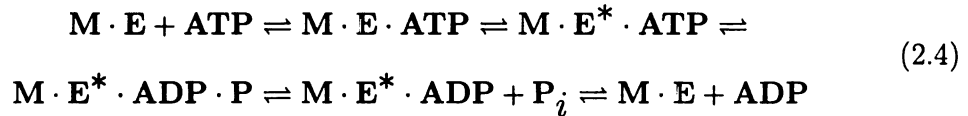
it is reasonable to postulate that T_{dP_i} is regulated by tensions. This is the other part in the updated rear-gated-head model [85]. The tension of the neck-linker enhances the release of P_i after the ATP molecule is hydrolyzed.

- T_{dP_i} depends on tensions and $T_{dP_i} \nearrow$ as tension \searrow .

Although these two models are not mutually exclusive, the front-gated-head model has obtained more support, especially because it is more consistent with new data [30]. Here our analysis shows that the rear-head-gated model should work with the front-gated-head to guarantee the processivity of kinesin.

2.4 Biochemical Reaction Cycle of Kinesin

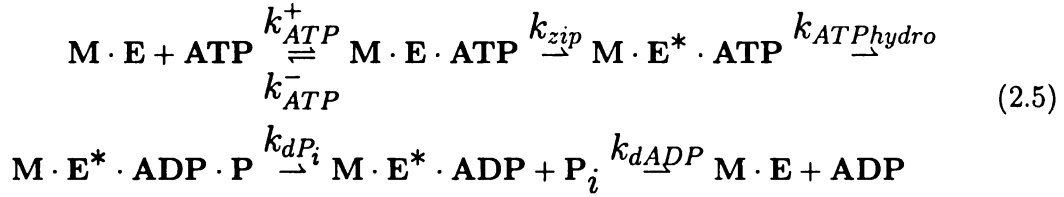
The biochemical reaction pathway of kinesin can be described as follows. **E** represents kinesin and **M** is the microtubule. **M·E** means that the kinesin is bound to the microtubule.



Here an ATP binding process is divided into two steps. First an ATP molecule arrives and binds to the catalytic core weakly and is easy to dissociate. If this weak binding induces a conformational change of the catalytic core, denoted by \mathbf{E}^* , then the ATP molecule is trapped into a tight binding state. After the ATP is trapped, it will go through the hydrolysis process. Theoretically every biochemical reaction is reversible. Because some reverse reaction rates of the hydrolysis process are very small, we ignore them and come up with the following biochemical reaction process for our model.

Reaction rate	s^{-1}
k_{dMT}^0	60
k_{ATP}^+	$3\mu M^{-1}s^{-1}$
k_{ATP}^-	150
k_{zip}^0	700
$k_{ATPhydro}$	100
$k_{dP_i}^0$	120
k_{dADP}	300

Table 2.1: The reaction rate constants



The neck-linker zipping takes place in the step where the ATP molecule is trapped, changing from the weak binding state to the strong.

The reaction rates used in the simulation are found from the other experimental results [18, 91] and the authors in [95] didn't measure these reaction rates.

Considering the regulation of the reaction rates by tension [32, 69], we adjust the reaction rates according to $k_{dMT} = k_{dMT}^0 e^{F\delta_c^1/K_B T}$, $k_{zip} = k_{zip}^0 e^{-F\delta_c^3/K_B T}$, $k_{dP_i} = k_{dP_i}^0 e^{F\delta_c^2/K_B T}$, where the force F is computed as a scalar by (2.9) and δ_c^i , $i = 1, 2, 3$ are the characteristic distances along the chemical reaction coordinates. In the simulation $\delta_c^1 = 0.7$, $\delta_c^2 = 2.0$, and $\delta_c^3 = 1.0$.

2.5 Tension Estimate of the neck-linkers

The estimate of the tension in the neck-linkers is critical in our modeling. The neck-linker is considered as an entropic spring, either a freely-jointed chain (FJC) or a worm-like chain (WLC) [32, 69]. When it is modeled as a FJC, the force-extension relation is determined only by the entropic effects. This is given by

$$F_{FJC}(x) = \frac{K_B T}{b} \frac{\frac{x}{\ell_c} (3 - (\frac{x}{\ell_c})^2)}{1 - (\frac{x}{\ell_c})^2}, \quad (2.6)$$

where b is the length of a monomer of the freely-jointed chain, x is the extension of the polymer, here computed as the end-to-end distance of the polymer, ℓ_c is the total length of the polymer, $\ell_c = Nb$ for a polymer with N monomers, K_B is Boltzmann's constant, and T is the absolute temperature.

If the neck-linker is treated as a worm-like chain which considers both the elastic and entropic effects of the polymer molecule in the force-extension formula. Then we have [69]

$$F_{WLC}(x) = \frac{K_B T}{\ell_p} \left(\frac{1}{4(1 - \frac{x}{\ell_c})^2} - \frac{1}{4} + \frac{x}{\ell_c} \right), \quad (2.7)$$

where ℓ_p is the persistence length of the polymer related to the material property and the shape of the cross section of the polymer. The persistence length of a polymer is a quantity used to measure how rigid the polymer is. Given a polymer chain, if we take a segment from it with the arc length ℓ_{arc} and the tangent angles of the two ends of the segment are denoted by θ_1, θ_2 , then we have the following formula for the correlation of these two angles [32, 69]

$$\langle \cos(\theta_1 - \theta_2) \rangle = e^{\frac{-\ell_{arc}}{2\ell_p}}.$$

Material types	$\ell_c(\text{nm})$	$\bar{\ell}_p(\text{nm})$	$s_n(\text{nm})$
Wild type	5.7	1.4	5.29
0P	6.84	1.4	5.86
2P	7.46	2.10	7.33
4P	8.08	2.28	7.95
6P	8.70	2.43	8.53
13P	10.87	2.82	10.33
19P	12.73	3.05	11.69
26P	14.90	3.25	13.13
14GS	12.16	1.08	7.08

Table 2.2: The total lengths, persistence lengths and natural lengths of the neck-linkers.

The correlation relation decays exponentially with the arc length ℓ_{arc} [32, 69]. In this thesis, the persistence lengths of the native neck-linker, the proline insertion and the GS insertion in the experiment are $\ell_p^{wt} = 1.4\text{nm}$, $\ell_p^{proline} = 4.4\text{nm}$, and $\ell_p^{GS} = 0.8\text{nm}$, [95]. The persistence length of the microtubule is about 1 mm.

When there is no external force applied to a worm-like chain, its mean square end-to-end length is given by [32, 69]

$$\langle R^2 \rangle = 2\ell_p^2 \left(e^{-\ell_c/\ell_p} - 1 + \frac{\ell_c}{\ell_p} \right) \quad (2.8)$$

The mean square end-to-end length of an FJC with N monomers is $\langle R^2 \rangle = Nb^2$, [22, 32, 69].

Molecular dynamics simulations [36] were used to estimate the internal tension stored in the neck-linker and found to be about 12-15 pN when both heads are bound. Calculation using (2.7) shows that the tension is 9.7 pN when the motor is in its two-head-bound state with $x = 8\text{nm}$ if we use $K_B T = 4.2 \text{ pN} \cdot \text{nm}$ and choose 15 as the total number of amino acids comprising each neck-linker. The experiments in [95] suggest that kinesin will easily dissociate from the microtubule when the applied external force is larger than around 10 pN. Therefore, we truncate the force of (2.7) at 25 pN.

In Table 2.2, the total length of one neck-linker is given for the wild type and each of the mutants. The persistence lengths and natural lengths are also given.

In the supplemental documents of [95], the authors used the length of each amino acid to be 0.38 nm and the length of a coil of the polyproline helix to be 0.31 nm in their computation. They did not include the lengths of the three amino acids, KKG, in their length estimate. In the thesis, we include KKG in the total length computation. Therefore the ℓ_C values in Table 2.2 are neither the same as the values in in Figure 2.1 nor the same as those in the supplemental documents of [95].

In the supplemental material of [95], they estimated the tension stored in the neck-linkers when the kinesin is in two-head-bound state. Some mistakes can be easily found in their computation. They used $\ell_C = 11.4\text{nm}$, $\ell_p = 1.4\text{nm}$, $x = 8 - \ell_n = 8 - 2.05 = 5.95 \approx 6$ and $K_b T = 4.1$ in (2.7), ℓ_n the natural length of the polymer, and found 3.9 pN as the tension for the kinesin in two head bound state with the neck-linker undocked. It is not clear how to arrive at 2.05 nm for ℓ_n . One possibility is that it is from $\sqrt{29 \times 0.38^2}$, which is the formula for the mean square end-to-end length of a freely-jointed chain and $29 = 15 + 14$ is the sum of the total number of amino acids for the 14GS mutants. They followed the same idea to estimate the tension when the neck-linker is docked.

It is easy to see that $F_{FLC,WLC}(\ell_C) = \infty$. This is consistent with the entropic nature of these forces because there is only one configuration when the extension equals the total length, corresponding to the minimal entropy state. Actually, for the worm-like chains, the entropic effect becomes dominant when the extension approaches to the total length. The entropic force is not a real force acting in the polymer but a quantity to describe a tendency for the polymer to restore to the maximal entropic state. Therefore it is not accurate to estimate the tension of neck-linkers by using the formulae (2.6) and (2.7) when the extension is large. A reasonable compromise is to cut off the force at 25 pN and to introduce the square root of the mean

square end-to-end length (2.8) as the natural length ℓ_n by modifying formula (2.7) as follows.

$$F(x) = \begin{cases} 0, & 0 \leq x \leq \ell_n \\ \frac{K_B T}{\bar{\ell}_p} \left(\frac{1}{4(1 - \frac{x - \ell_n}{\ell_c - \ell_n})^2} - \frac{1}{4} + \frac{x - \ell_n}{\ell_c - \ell_n} \right), & x \geq \ell_n \\ 25, & F(x) \geq 25 \end{cases} \quad (2.9)$$

where $\bar{\ell}_p$ is the effective persistence length of the neck-linkers of the mutants and is computed by

$$\bar{\ell}_p = \ell_p^{wt} \frac{\ell_c^{wt}}{\ell_c} + \ell_p^{mutant} \frac{\ell_c^{mutant}}{\ell_c}. \quad (2.10)$$

If two neck-linkers of the mutants are viewed as a whole worm-like chain, then the natural length is calculated as the square root of $\langle R^2 \rangle$:

$$\ell_n = \sqrt{\langle R^2 \rangle} = \sqrt{2\bar{\ell}_p^2 \left(e^{-2\ell_c/\bar{\ell}_p} - 1 + \frac{2\ell_c}{\bar{\ell}_p} \right)}, \quad (2.11)$$

which is shown in Table 2.2.

In our simulation, we model the motion of the tethered head in three-dimensional space. The formula (2.9) only gives us the magnitude of the force. We use \mathbf{X}_{H1} to denote the position vector of the tethered head and \mathbf{X}_{H2} to denote the position vector of the bound head. The extension x in (2.9) is equal to Euclidean norm of the vector $\mathbf{X}_{H2} - \mathbf{X}_{H1}$, i.e., $x = \|\mathbf{X}_{H2} - \mathbf{X}_{H1}\|$. The orientation is $\hat{n} = \frac{\mathbf{X}_{H2} - \mathbf{X}_{H1}}{\|\mathbf{X}_{H2} - \mathbf{X}_{H1}\|}$. Therefore the force vector acting on the tethered head is

$$\mathbf{F}(\mathbf{X}_{H1}) = F(x)\hat{n} \quad (2.12)$$

Material types	$\bar{\kappa}$ (pN/nm)	l_n (nm)
Wild type	0.91	5.29
0P	0.91	4.92
2P	0.65	4.99
4P	0.50	5.20
6P	0.41	5.47
13P	0.25	6.98
19P	0.19	8.38
26P	0.14	10.05
14GS	0.56	6.21

Table 2.3: The spring constants and the natural lengths of the neck-linkers

The neck-linker can also be approximated as a linear spring, in which the restoring force is the product of the spring constant and the extension relative to the natural length. The spring constant can be estimated from the linearization of (2.7), using κ to denote the spring constant, $\kappa = \frac{\partial F(x)}{\partial x}|_{x=0} = \frac{3K_B T}{2\ell_c \ell_p}$. A spring composed of two different materials, with the spring constants κ_1 and κ_2 , has an effective spring constant

$$\bar{\kappa} = \frac{\kappa_1 \kappa_2}{\kappa_1 + \kappa_2}. \quad (2.13)$$

The formula (2.10) can be derived from (2.13) as follows. For the extended neck-linker of the mutant kinesin, denote its effective persistence length by $\bar{\ell}_p$. According to (2.13), we have

$$\frac{3K_B T}{2\ell_c \bar{\ell}_p} = \frac{\frac{3K_B T}{2\ell_c^{wt} \ell_p^{wt}} \frac{3K_B T}{2\ell_c^{mutant} \ell_p^{mutant}}}{\frac{3K_B T}{2\ell_c^{wt} \ell_p^{wt}} + \frac{3K_B T}{2\ell_c^{mutant} \ell_p^{mutant}}}. \quad (2.14)$$

The formula (2.10) is obtained by solving (2.14) for $\bar{\ell}_p$.

The engineered neck-linker of kinesin mutants can be idealized as a freely-jointed chain composed of the inserted part and the native part that are treated as worm-like chains, but freely jointed to each other. This treatment gives the following formula

for the natural length of the neck-linkers of the mutants.

$$l_n = \sqrt{2 \langle R^2 \rangle_{wt} + 2 \langle R^2 \rangle_{mu}} \quad (2.15)$$

$$F(x) = \begin{cases} 0, & 0 \leq s \leq l_n \\ \bar{\kappa}(x - l_n), & x \geq l_n \end{cases} \quad (2.16)$$

Using the above formulas, we have the parameter values for the spring constants and natural length in Table 2.3.

For the wild type kinesin, we model its two neck-linkers as a whole worm-like chain and the natural length is equal to

$$\ell_n^{wt} = l_n^{wt} = \sqrt{2\ell_p^2 \left(e^{-2\ell_c/\ell_p} - 1 + \frac{\ell_c}{\ell_p} \right)}. \quad (2.17)$$

2.6 Algorithm

The whole simulation process can be described as follows. Here, ζ is used to denote different random numbers with uniform distribution between 0 and 1.

1. Head1 dissociation

- Start from a two-head-bound state on the microtubule, with the leading head (the head close to the plus end of microtubule) in its nucleotide free state and the trailing head in its ADP bound state, see figure 2.4 and 2.5.
- Head1 dissociation. Test for the random dissociation of head1 from the microtubule and ATP binding in head2. The neck-linker zipping induced by ATP binding in head2 may or may not imply the detachment of head1 from the microtubule depending on the length of neck-linkers.

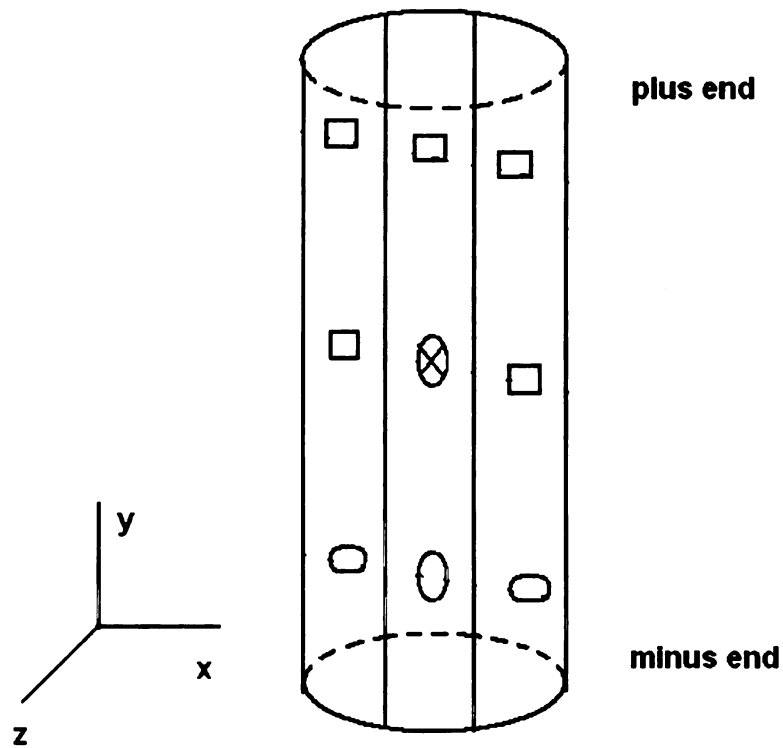


Figure 2.5: Illustration of the binding sites for the wild type kinesin. Three vertical stripes represent three protofilaments of the microtubule. Assume that kinesin can only bind to the sites on these three neighboring protofilaments. The oval with X inside denotes the bound head, i.e., head2 in the algorithm and the dark head in Figure 2.4. The oval represents head1 in the algorithm, the light head in Figure 2.4. The five forward binding sites for head1 are represented by squares. The number of binding sites for the mutants will increase depending on the reachable range of head1 of the mutants. Notice that the binding sites are arranged to reflect the helical structure of the microtubule.

2. Tethered diffusion.

- Head1 experiences a 3D diffusion process during which it might bind to a rearward binding site. If so, this binding is weak and head1 will detach again. If head1 diffuses to a forward binding position and binds to it, then it can release ADP rapidly, bind to the microtubule strongly and completes a step.
- The movement of the tethered head is modeled by a Langevin equation. Let \mathbf{X}_{H1} be the position vector of the tethered head. Newton's second law gives the equation for the motion of \mathbf{X}_{H1} :

$$m\ddot{\mathbf{X}}_{H1} = -\gamma\dot{\mathbf{X}}_{H1} + \mathbf{F}(\mathbf{X}_{H1}) + \sqrt{2K_B T \gamma} \frac{dW}{dt}, \quad (2.18)$$

where m is the mass of the head and γ is the drag coefficient. $\frac{dW}{dt}$ represents white noise and $W(\mathbf{X}_{H1}, t)$ is Brownian motion. $\mathbf{F}(\mathbf{X}_{H1})$ is the sum of the entropic force and any external force acting on the head. The external force in our simulation is zero and the entropic force is computed by (2.12). The order of magnitude of the mass is 10^{-17} and the inertial time scale is defined as m/γ and $m/\gamma \approx 10^{-10}s$, which is so small that the inertial term can be ignored. The above equation becomes a Langevin equation

$$\gamma\dot{\mathbf{X}}_{H1} = \mathbf{F}(\mathbf{X}_{H1}) + \sqrt{2K_B T \gamma} \frac{dW}{dt}. \quad (2.19)$$

Solving this stochastic differential equation by using the Euler scheme, we have the following iteration formula for (2.19) from t^n to $t^{n+1} = t^n + dt$,

$$\mathbf{X}_{H1}^{n+1} = \mathbf{X}_{H1}^n + \frac{1}{\gamma} \mathbf{F}(\mathbf{X}_{H1}^n) dt + \sqrt{2Ddt} (W^{n+1} - W^n) \quad (2.20)$$

where we have used Einstein relation $D = \frac{K_B T}{\gamma}$.

- When the distance between the tethered head and some binding site is less than a given threshold, $r_{cutoff} = 2.5$, a binding probability is considered by using the following formula:

$$P_{binding} = \begin{cases} e^{-\beta d^2 \cos\theta}, & \text{wild type} \\ e^{-\beta d^2 (\cos\theta)^2}, & \text{mutants} \end{cases} \quad (2.21)$$

where d is the distance between the tethered head and the binding site and $\cos\theta = v_1 \cdot v_2$, where v_1 is the orientation of the plus end of the microtubule and v_2 is the orientation of the binding site to head2. $\beta = 1.5$ is used in the simulation to approximate the swing process of head1 induced by the neck-linker docking.

Other binding probability formulas are tested. The following one is to model the binding through the electrostatic attraction:

$$P_{binding} = P_d P_O, \quad (2.22)$$

where

$$P_d = \begin{cases} 1, & d \leq 0.1 \\ 1 - c_1 e^{-\frac{c_2}{K_B T d}}, & 0.1 \leq d \leq 2.5, \end{cases} \quad (2.23)$$

and $P_O = e^{-c_3 |\sin(\alpha/2)|}$, where $\alpha = \theta + c_4 \frac{\ell_c - s}{\ell_p} \omega$ and ω is a random variable with a normal distribution of mean zero and standard deviation one. c_1 and c_2 are chosen to make (2.23) a continuous function. We used $c_1 = 1.3$ and $c_2 = -4.2 r_{cutoff} \ln(1/c_1)$.

- The chemical state of head2 stochastically update. If it has not bound

an ATP, then continue to test for random ATP binding and then neck-linker zipping in head2. The random test of ATP binding is as follows. If $\zeta < k_{ATP}^+[ATP]dt$ is true, then an ATP molecule binds to the catalytic core of head2, where $[ATP]$ represents the concentration of ATP. If ATP has bound, then test for random ATP hydrolysis and Pi release until head2 arrives at the ADP bound state.

- When head2 is in its ADP state after ATP hydrolysis, kinesin may fall off or just release the bound ADP molecule. If head1 happens to be in a rearward bound state, then head2 will either release the ADP molecule and not unbind from the microtubule or stay in its ADP bound state for the next update. If head1 is in the tethered diffusion state, head2 will either release the ADP or possibly unbind from the microtubule depending on the relative position of head1 to head2. Let the positive direction of y in (x, y, z) coordinates point to the plus end of microtubule, (see Figure 2.5). $X_{H1}^y(t_n)$ and X_{H2}^y are the y-coordinate of head1 and head2 at time t_n . If $X_{H1}^y(t_n) \leq X_{H2}^y + C_{gating}l_C$, then ADP release in the head2 is considered, i.e., that random event is tested. We use $C_{gating} = 0.2$ in the simulation. Otherwise unbinding of head2 will compete with the ADP release in head2. If unbinding of head2 takes place, then the kinesin falls off. If the ADP is released in head2, then a futile ATP hydrolysis cycle is recorded.

3. Forward binding.

- $P_{binding}$ is tested against a random number in $[0, 1]$ and if it is greater, then head1 binds to the binding site immediately.
- After head1 binds to a forward binding site, it releases the ADP quickly and then is in a strong binding state. Head2 continues the process from

step 2 and eventually arrives in the ADP state. Next ATP binding does not occur in head1 until ATP hydrolysis is complete in head2 and head2 is in a weak binding state. Now the head1 and the head2 have exchanged their trailing and leading roles and are ready for a new step.

To compute the average speed and run length of kinesin and its mutants, we run 5000 chemomechanical cycles for each of them. All the continuous paths are detected from those 5000 steps and assume that there are N_{path} continuous paths. The run number, N_{rn} , of a path is defined as the total number of steps in this continuous path and the run length, L_{run} , of it is defined as the total distance traveled. Three different ways are used to compute the average speed. The first formula is given by

$$V_1 = \frac{\text{The total distance traveled in } N_{path} \text{ paths}}{\text{The total time spent in } N_{path} \text{ paths}} \quad (2.24)$$

For each path, we find the corresponding run number and its median value of all the run numbers, N_{rn}^{median} .

$$V_i = \frac{\text{The length of the } i^{th} \text{ path with } N_{rn} \geq N_{rn}^{median}}{\text{The corresponding time for the } i^{th} \text{ path}} \quad (2.25)$$

$$V_2 = \langle V_i \rangle, \text{ over all the paths with } N_{rn} \geq N_{rn}^{median} \quad (2.26)$$

To compare the result of run length between the simulation and the experiment, we follow the method used in supplemental material in [95] where the mean run length is defined as follows.

$$L_{run}^{mean} = \frac{\sum_{L_{run} \geq 500} L_{run}}{\text{The total number of the paths with } L_{rn} \geq 500} \quad (2.27)$$

The third way to compute the speed is

$$V_3 = \left\langle \frac{\text{The length of the } i^{th} \text{ path with } L_{run} \geq 500}{\text{The corresponding time for the } i^{th} \text{ path}} \right\rangle, \quad (2.28)$$

The average speed calculated from these three different definitions are very close, see Figure 2.6.

2.7 Simulation Results

First of all, the ratio of the speed of the kinesin to the concentration of ATP is calculated and the result with the Michaelis-Menton chemical kinetics, (see Figure 2.7).

Mutants with extended neck-linkers have smaller tension when taking an 8 nm step and so they tend to take more time to detach from the microtubule, according to the rear-gated head hypothesis. Also the long neck-linker mutants can reach more backward binding sites so that they may have more backward temporary binding. More backward binding needs more time for them to dissociate from the microtubule. Our result supports this conclusion, Figure 2.8 showing clearly the average dwelling time to be an increasing function over the mutants. Here the dwelling time is defined as all the time when head1 is not in the diffusion state in one chemomechanical cycle.

Our detailed simulation of the stepping process of kinesin and its mutants with extended neck-linkers has reproduced the experimental results qualitatively. There are mainly two differences between our simulation results and the experimental outcomes. The magnitude of the speed from the simulations is large although it does clearly show the small speed for the mutants with the longer neck-linkers. The second difference is that the speed of 14GS is larger than the speed of 19P and (or) 26P in some simulations.

Speed in Figure 2.10 shows the decreasing tendency as is seen in the experimental result. In our simulation, the speed among the mutants 13P,19P,26P and 14GS does

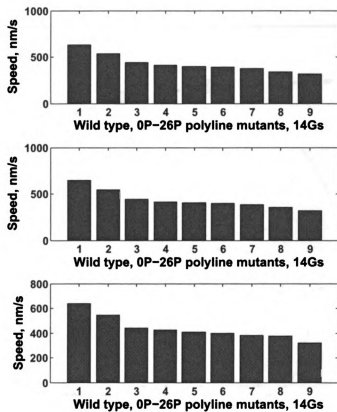


Figure 2.6: Speed of the wild type, 0P-26P and 14GS mutants computed by formulas (2.24, 2.26, 2.28)

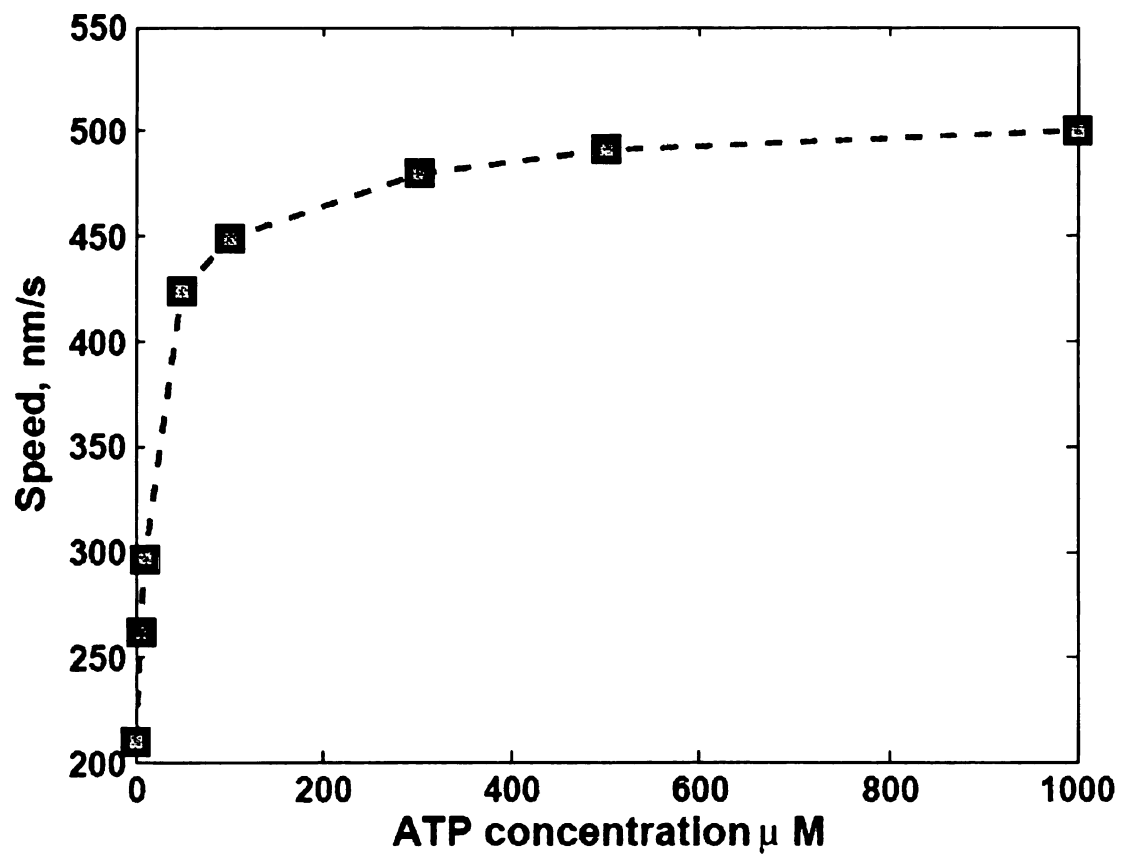


Figure 2.7: The speed of wild type kinesin vs ATP concentration (μM)

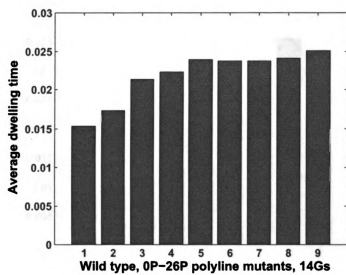


Figure 2.8: The average dwelling time of the wild type, 0P-26P and 14GS mutants

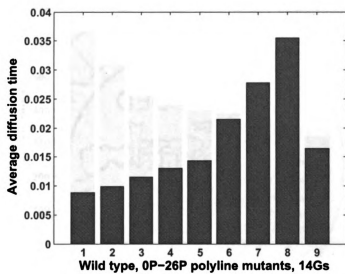


Figure 2.9: The average diffusion time of the wild type, 0P-26P and 14GS mutants

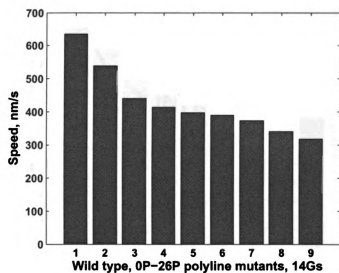


Figure 2.10: Speed of the wild type, 0P-26P and 14GS mutants

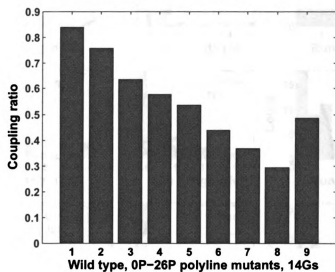


Figure 2.11: Coupling ratio of the wild type, 0P-26P and 14GS mutants

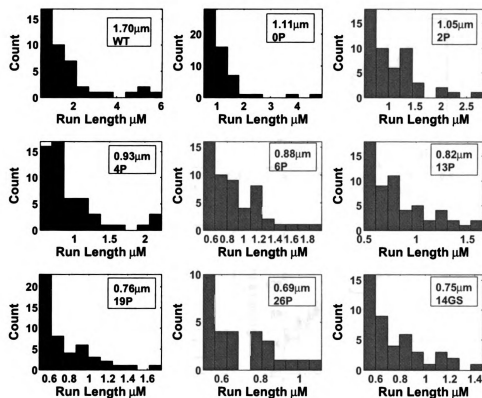


Figure 2.12: Runlength of the wild type, 0P-26P and 14GS mutants. The mean run length is shown in the insets.

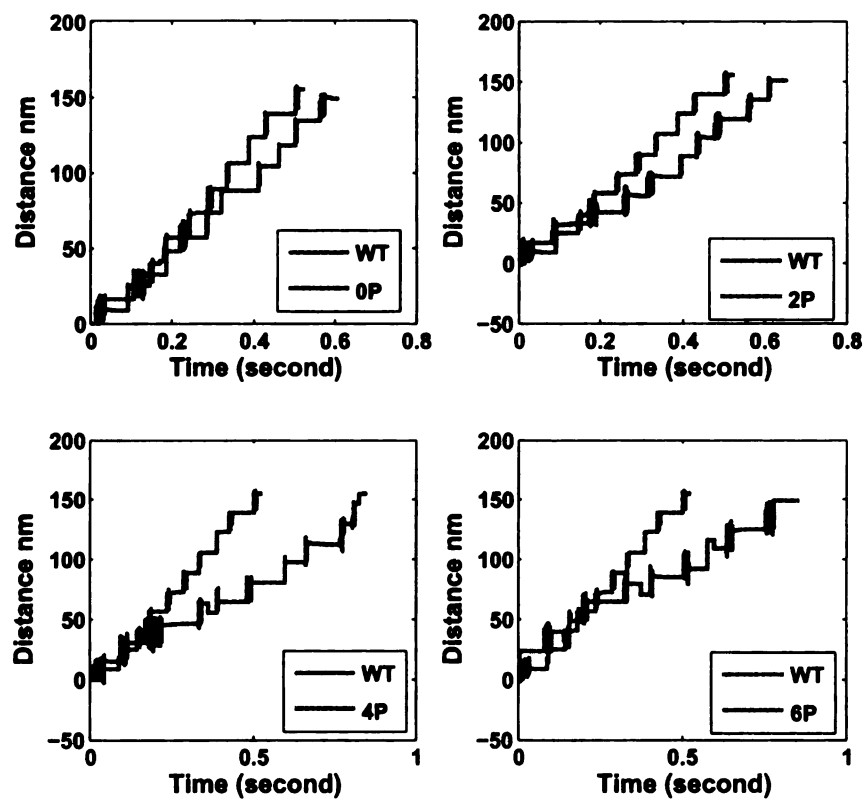


Figure 2.13: Trajectory samples of wild type kinesin and 0P, 2P, 4P and 6P mutants.

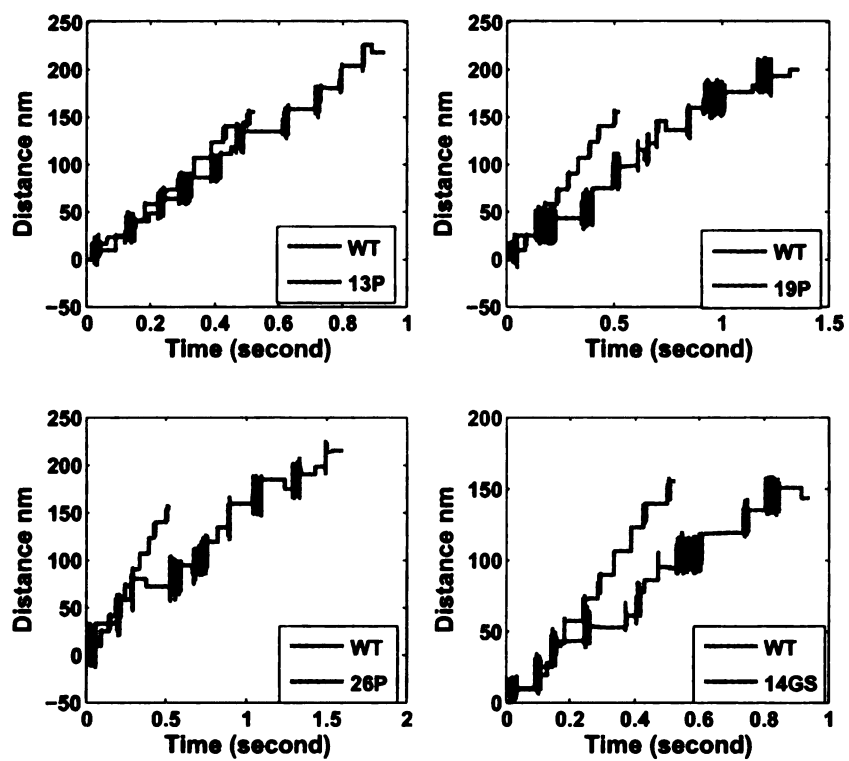


Figure 2.14: Trajectory samples of wild type kinesin and 13P, 19P, 26P and 14GS mutants.

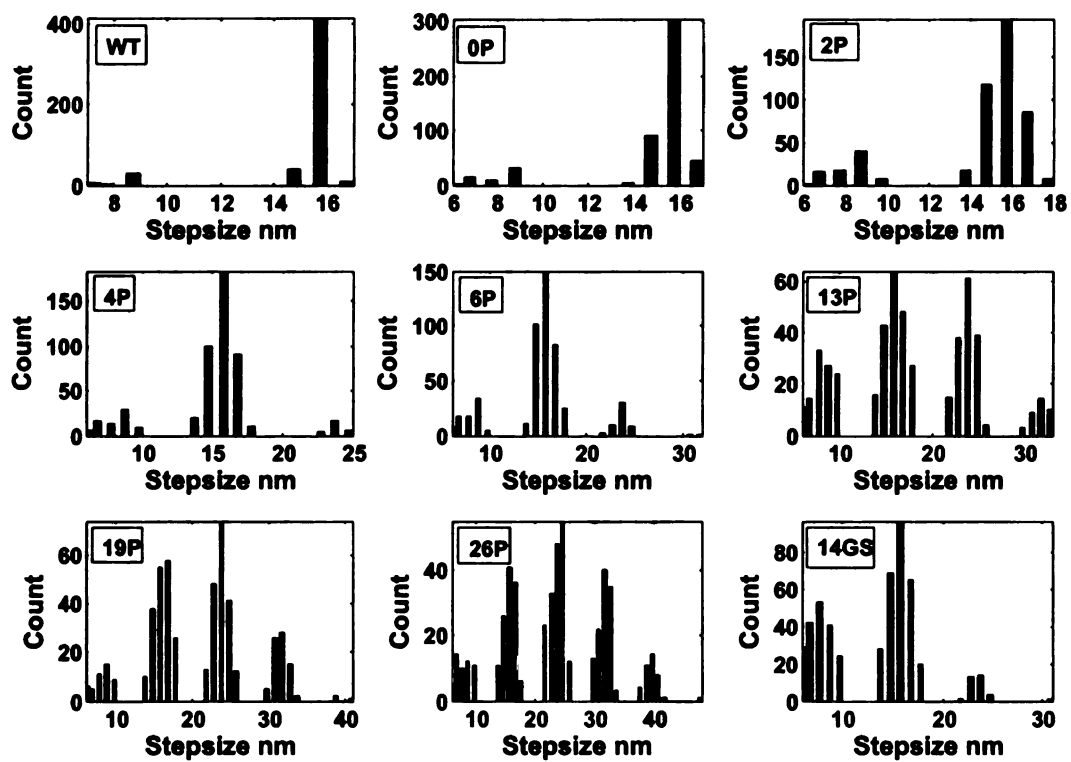


Figure 2.15: Stepsize histogram of the wild type and mutant kinesins.

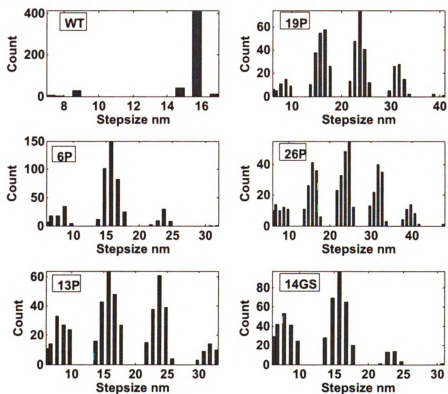


Figure 2.16: The histogram of stepsize from the simulation results for the wild type, 6P, 13, 19P, 26P, and 14GS mutants. The histograms of experimental results are shown in Figure 2.15.

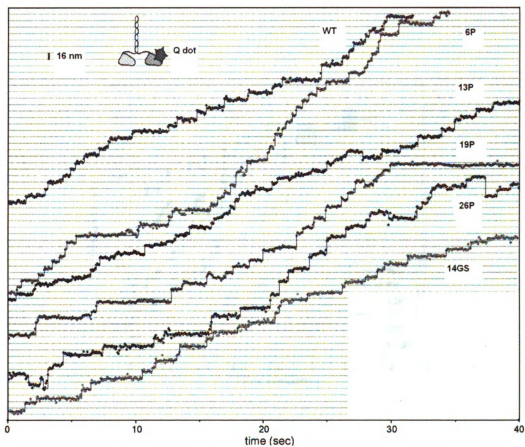


Figure 2.17: Trajectory samples of wt, 6P, 13P, 19P, 26P, and 14GS from the experimental results. These trajectories have more or less the same slope because they are obtained from different ATP concentrations. See the simulation results in Figure 2.18

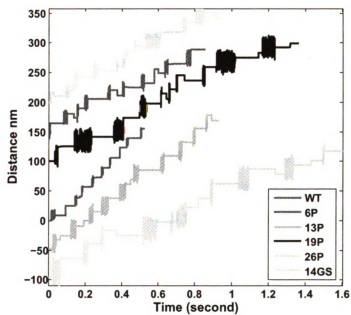


Figure 2.18: Simulation results for the trajectories of wt, 6P, 13P, 19P, 26P, and 14GS. The same ATP concentration, 1 mM, is used in the simulation. See the experiment trajectories in Figure 2.17

not decrease dramatically and seems more or less to be the same. One of the possible reasons is that the tension of 14GS calculated by (2.9) is actually larger than that of 19P and 26P and this large tension comes from the entropy effect of 14GS since it is softer, i.e., with a small persistence length. We also observed from Figure 2.2 that the 14GS mutant has more small step lateral walking. The extended neck-linker length of 14GS is 12.13 nm, very close to 12.76 nm, the neck-linker length of 19P, but the histogram, Figure 2.15, of 14GS is different from that of 19P where 14GS does not have a peak at 24 nm. We tested an idea to reduce the entropy effect so that the speed of 14GS may become small. We use the binding probability of 14GS $P_{binding} = e^{-\alpha d^2}$ which only considers the attraction distance without considering the orientation term $\cos\theta$ in (2.21). This consideration comes from the observation of the histogram of 14GS in which there are more small lateral steps because the soft 14GS segment in the neck-linker makes the mutant much more flexible so that it can more likely bind to the lateral binding sites. With this modification, the speed of 14GS becomes smaller than the speeds of 19P and 26P mutants.

The trajectory samples are shown in the Figures 2.13 2.14 and 2.18. Each sample represents the trajectory of a ten-step run of one head of the kinesin. Because those samples are taken randomly, the slopes of these trajectories do not represent the average speeds of each type of kinesin, which is shown in the Figure 2.10. The results in the Figures 2.13 and 2.14 indicate that the speed of wild type is greater than that of the mutants.

The histograms of step sizes of all motors are shown in the Figure 2.15. The simulation results are shown in the Figure 2.16. The simulation results are consistent with the experimental results when any backward walking is ignored.

2.8 Discussion

In the front-gated head hypothesis, it is suggested that ATP does not bind to the empty front head until the rear head dissociates from the microtubule [77]. If we assume that the movement of the tethered head is purely diffusional, then this front-gated head assumption may lead to a forward step of kinesin without consuming an ATP molecule. Indeed, a kinesin head can be seen as a sphere of radius around 3 nm. According to the Stokes' law [32], the diffusion constant of such a sphere is around $D = 6.7 \times 10^7 \text{ nm}^2/\text{s}$, which is very close to a reported experimental measured value $D = 2.24 \times 10^7 \text{ nm}^2/\text{s}$. For wild type kinesins, they mainly walk on the axis of a protofilament so the walking can be modeled as one dimensional diffusion process. For a 1D diffusion, if the particle is not subject to external forces, the first passage time [32] is equal to $t_{fp} = \frac{d_{step}^2}{D}$, which gives the average time for the tethered head to diffuse through the distance d_{step} and bind to a front binding site, completing one step. Next we examine what the probability is for the motor to bind an ATP molecule during the period t_{fp} . In consideration of the diffusion constant, the time step size used in the simulation is $dt = 10^{-8}$ second. Correspondingly, the first passage time t_{fp} needs around $N_{step} = \left\lceil \frac{t_{fp}}{dt} \right\rceil = 1143$ time steps. On the other hand, on average, the probability of an ATP molecule to bind is $q = dt[\text{ATP}]k_{ATP}^+ = 10^{-8} \times 3 \times 10^3 = 3 \times 10^{-5}$ when $[\text{ATP}]$ is $1000\mu\text{M}$ and k_{ATP}^+ takes the value in Table 2.1. Given $N_{step} = 1143$, the probability for the kinesin to bind one ATP molecule is $1 - (1 - q)^{N_{step} + 1} = 1 - (1 - 3 \times 10^{-5})^{1144} = 0.034$. This result indicates that the diffusion is so fast that the kinesin could have finished one forward step even without an ATP binding, not to mention neck-linker docking. Block in [11] pointed out that it takes less than $100\mu\text{s}$ for a kinesin to finish a diffusive search process. A time of $100\mu\text{s}$ corresponds to 10000 iteration steps. Given $N_{step} = 10000$, the probability for the kinesin to bind one ATP molecule is

$1 - (1 - q)^{10001} = 1 - (1 - 3 \times 10^{-5})^{10001} = 0.26$, which is much larger than 0.034 but it is still not large enough. Therefore this simple calculation suggests it is unlikely for the empty front bound head not to bind ATP molecules until the rear head unbinds from the microtubule and starts a diffusive process.

To solve this puzzle, we may assume that the front bound head of the kinesin begins ATP binding before the rear head detachment. The timing point may be reasonably assumed at the moment when the P_i is released and the rear head is in the weak binding state. This assumption does not conflict with the result from [56] where kinesin spends most time of a cycle in a two-head-bound state and it quickly moves to the next front binding position in company with the ATP binding when there is a high ATP concentration. Certainly another scenario is that the rear head remains parked somewhere after it unbinds from the microtubule and rapidly swings to a forward site with a force provided by the neck-linker docking that is induced by ATP binding. This is the polymer gating mechanism in [1, 7, 27] where the tethered head parks in front of the microtubule bound head and does not bind to the tubulin until an ATP binds to the bound head. But the data in [56] suggest that the tethered head parks behind the bound head instead of in the front of it. Surely, more experiments are expected to elucidate the details of the polymer gating.

The movement of the tethered head is believed to involve a swing process induced by the neck-linker docking. The experiments [56, 95] suggest that kinesin spends most of the time in a two-head-bound state and it quickly swings to the next binding site when the neck linker is zipped induced by the ATP binding. To model this process, we suggest an idea where an overdamped beam equation may be employed to describe this swing movement. We consider the neck-linkers as an elastic beam, in which the potential is stored when the kinesin is in the two-head-bound state in which we postulate that the neck-linkers are somehow twisted. And this is where the stored potential energy may reside. When the tethered head unbinds from the microtubule,

the released potential, coming from the release of the strain, immediately changes the orientation of the tethered head such that it cannot easily bind back to the initial site again and throws the tethered head to the next front binding position. We may set the root of the neck-linker in the bound head at the arclength 0 and the the root of the neck-linker in the tethered head at arclength ℓ_C . We need to determine the appropriate boundary conditions to describe these two end points in the swing process. This is a future direction of our work.

Chapter 3

Interactions between Microtubules and Molecular Motors

3.1 Essentials of the Model

We model microtubules as stiff polar rods of equal length l exhibiting anisotropic diffusion in the plane. Diffusion of the rod is characterized by three diffusion coefficients, diffusion parallel to the rod orientation D_{\parallel} , perpendicular to its orientation D_{\perp} , and rotational diffusion D_r . In the following we assume $D_{\parallel} = 2D_{\perp}$ [22] for stiff rods diffusing in a viscous fluid.

The key ingredient in the theory proposed in Refs.[2, 3] was the approximation of the complicated process of interaction of one molecular motor with two microtubules by a simple instant alignment process, see Fig. 3.1. We focus on the two dimensional situation, and describe the orientation of microtubules by the planar angles $\varphi_{1,2}$. The microtubules before the collision possess initial angles $\varphi_{1,2}^b$. The action of the molecular motor binding simultaneously to two microtubules results in their mutual alignment, and the angles after interaction become

$$\varphi_1^a = \varphi_2^a = \frac{\varphi_1^b + \varphi_2^b}{2}. \quad (3.1)$$

By analogy with the physics of inelastically colliding grains, we call this kind of process fully inelastic collision (see e.g. [4]). Such an inelastic collision is a simple and reasonable approximation of the complicated interaction process [3], and is, in fact, an effect of simultaneous action of several motors or motors and static crosslinking polymers. An analysis of the interaction of two stiff rods with one motor shows that the overall change in the angle between the rods is rather small: the angle decreases only by 25-30 % on average [3, 43]. However, simultaneous action of a static crosslink, serving as a hinge, and a motor moving along both filaments results in a fast and complete alignment of the filaments [97]. This justifies the assumption of fully inelastic and instantaneous collisions for the rods interaction. Complete alignment also occurs for the case of a simultaneous action of two motors moving in the opposite directions, as in the experiments with kinesin-NCD (glutathione-S-transferase-nonclaret disjunctional fusion protein) mixtures [81]. The same is true of two motors of the same type moving in the same direction but with different speeds, where the variation in speed is due to the variability of motor properties and the stochastic character of the motion.

We set the molecular motor concentration m to be uniform in space. This assumption is not satisfied in reality in the presence of defects such as asters or vortices. Since the motor convection along the filaments is faster than thermal diffusion, the motors tend to congregate at the aster or vortex centers. However, as shown in [3], the motor inhomogeneity has only a *quantitative* effect on the self-organization process near a phase transition and does not affect the qualitative features, such as the morphology or the phase diagram and the nature of the transitions. If it were necessary, however, the effects of large-scale motor distribution inhomogeneities could be easily incorporated into our model by modification of the interaction rules according to the local

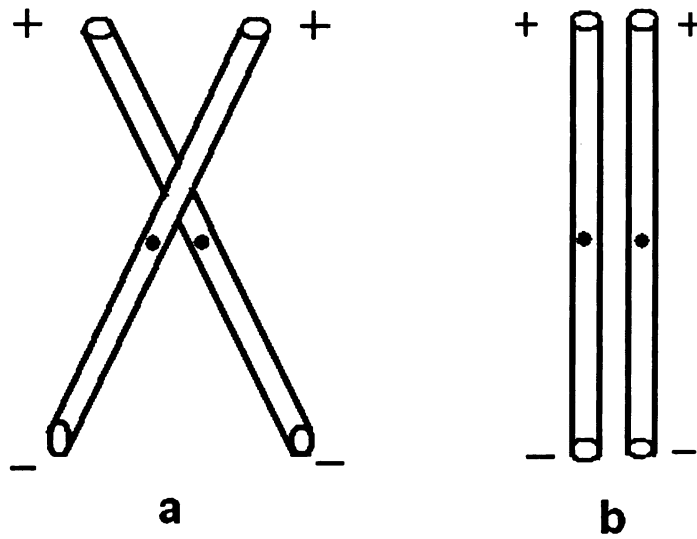


Figure 3.1: Schematics of an alignment event (inelastic collision) between two microtubules interacting with one multi-headed molecular motor. The black dots represent the center of mass of the microtubules. (a) A multi-headed molecular motor cluster attached at the intersection point of microtubules moves from the negative (-) towards the positive (+) end of the microtubules. (b) After the interaction, the orientational angles $\varphi_{1,2}$ and the corresponding positions of the midpoints $\mathbf{R}_{1,2}$ become aligned.

density and orientation of microtubules. At the same time, the assumption of motor homogeneity significantly simplifies the calculations. In the future we plan to study the effect of motor convection explicitly.

This assumption is justified by a large value of the motor diffusion D_m compared to the microtubule diffusion, $D_m \approx 20\mu m^2/s \approx 500D_{||}$. Due to the advection of the motors along the microtubules there is some accumulation of motors at the centers of asters and vortices, (see e.g., [63]). However, for a typical motor speed of $v \approx 1\mu m/s$ and the microtubule length $l \approx 1\mu m$, the (effective) Péclet number $Pe = \frac{vl}{D} \approx 0.05$, implying that diffusion dominates advection.

The motor concentration m affects the probability of interaction P_{int} between two microtubules in a given period of time Δt . In the following we set $P_{int} \sim \sigma^2 m \Delta t$, where σ^2 is the effective interaction cross-section. The value of $\sigma \approx 30 - 50$ nm, the order of size of a kinesin-type molecular motor.

In addition, we assume that the interaction probability P_{int} depends on the position of the intersection point, see Figure 3.1. The intersection position is indicated by the signed distance $s_{1,2}$, $-\frac{l}{2} \leq s_{1,2} \leq \frac{l}{2}$, from the midpoint of each rod. According to Refs. [2, 3], due to the polar nature of the microtubules, the dependence of the interaction probability on the intersection (and, correspondingly, the attachment position) results in an anisotropic probability kernel in the collision integral in the master equation. The anisotropy of the kernel, characterized by the parameter β , ranging between -1 and 1, depends on the motor dwelling time t_{end} , which is small for kinesin-type motors and large for NCD-type motors. In Ref. [3] the relation between the kernel anisotropy β and the motor dwell time at the end of the microtubule t_{end} in the limit of $t_{end} \gg 1$ was estimated as follows: $\beta \sim (v - const/t_{end})/p_{off}$, where v is the motor speed, p_{off} is the motor unbinding rate. Thus, one sees that β increases with the increase in t_{end} . In contrast, the motor attachment rate p_{on} has little effect on the kernel anisotropy, in agreement with experiments [62, 63]. As

was shown in Refs. [2, 3], the anisotropy parameter controls the transition between asters and vortices; in the continuum model no vortices were observed for large values of the kernel anisotropy.

In order to accommodate the anisotropy effects, that is, dwelling of the motors at the end of microtubules, in our model we introduce the following dependence of interaction probability on the attachment positions:

$$P_{int} = P_0 \left(1 + \beta \frac{s_1 + s_2}{l} \right). \quad (3.2)$$

Here the parameter $P_0 = Cm\sigma^2\Delta t$ encodes the aforementioned dependence of the interaction probability on the motor concentration m , the interaction cross-section σ and the elapsed time Δt (here C is a constant). Since σ is a fixed physical parameter, and Δt is fixed throughout our simulations (see below), the range of parameter values $0 < P_0 \leq 0.5$ reflects different values of the uniform motor concentration m . The value (and the sign) of the other parameter, β , depends on the type of motor. We believe that this generic linear dependence on the distances $s_{1,2}$ captures the qualitative effects of the kernel anisotropy. Our experiments with different dependencies of the probability P_{int} on $s_{1,2}$ yielded qualitatively similar results.

After the interaction we postulate that not only the angles, but also the midpoint positions of the microtubules $\mathbf{R}_{1,2}$ coincide

$$\mathbf{R}_1^a = \mathbf{R}_2^a = \frac{\mathbf{R}_1^b + \mathbf{R}_2^b}{2}. \quad (3.3)$$

This approximation is reasonable in the case of large dwelling times t_{end} of the motors, which guarantees that after the interaction the *end points* of the microtubules will coincide. Then, together with the alignment interaction, this effect will justify the assumption on the alignment of the midpoints as well. A large value of the dwelling

time t_{end} is a reasonable approximation for NCD motors, however t_{end} is small for kinesin-type motors. As we will show later, the midpoint alignment assumption may produce under some conditions specific effects, such as layering of the microtubules, or “smectic ordering” [20]. In our future work we plan to introduce more realistic rules for the midpoint displacements.

3.2 Algorithm Description

We performed simulations on a two-dimensional square domain with periodic boundary conditions. Initially, microtubules are randomly distributed over the domain. At each time step, (e.g., from t_n to t_{n+1}), the update of the positions and orientations of the microtubules is comprised of one substep processing anisotropic diffusion and one substep processing inelastic collision. The total timestep size was set at $\Delta t = 0.1$.

The diffusion of rigid rods in a viscous fluid is characterized by three diffusion coefficients, parallel D_{\parallel} , perpendicular D_{\perp} and rotational D_r . We used the following relations between the diffusion coefficients from Kirkwood’s theory for polymer diffusion in three dimensions, $D_{\parallel} = 2D_{\perp}$, $D_r = \frac{c}{l^2} D_{\parallel}$. We used $c = 1.5$ and $l = 0.5$ in our simulation. For a three-dimensional fluid the coefficient $c \approx 24$ [22]. However, the value of c rapidly decreases for quasi-two dimensional thin film and membranes, see [53]. We verified that the value of coefficient c does not change the qualitative behavior of the system, it affects only the position of the transition points. The “diffusion substep” is introduced as an anisotropic random walk of the microtubules’ center position $\mathbf{R} = (x, y)$ and random rotation of its orientation φ . The positions and orientations are updated at each such substep as follows:

$$\begin{aligned}
\mathbf{R}_{n+1} &= \mathbf{R}_n + \zeta_1 \Delta_{\parallel} \mathbf{U}_n + \zeta_2 \Delta_{\perp} \mathbf{N}_n \\
\varphi_{n+1} &= \varphi_n + \zeta_3 \Delta r
\end{aligned} \tag{3.4}$$

where $\zeta_i \in (-0.5, 0.5)$ are three uniform random numbers generated each time, and $\Delta_i = \sqrt{24 D_i \Delta t}$, where D_i is either D_{\perp} , D_{\parallel} or D_r , and vectors $\mathbf{U}_n = (\cos \varphi_n, \sin \varphi_n)$, $\mathbf{N}_n = (-\sin \varphi_n, \cos \varphi_n)$ are directed along (U) and perpendicular (N) to the orientation of the microtubule. The factor 24 in the expression for Δ_i ensures that the effective diffusion has the correct value of D_i based on the variance of ζ_i .

At the “collision step”, after diffusion, we check whether any pairs of microtubules intersect, and if so we locate the intersection points of the microtubules and assign an interaction probability to those pairs according to (3.2). In all of those intersections, some of them are simple binary intersections, but others may be multiple intersections, that is, a microtubule intersecting with more than one other microtubule. Certainly, at a low density of microtubules binary collisions are more typical. Regardless of whether intersections are binary or multiple, we calculate all interaction probabilities and sort them in descending order. Starting with the greatest P_{int} , we compare it with a randomly generated number $\zeta_4 \in [0, 1]$. If $P_{int} > \zeta_4$, then we update that pair of microtubules according to the collision rules Eqs.(3.1) and (3.3). If either of these two microtubules had other intersections, they are ignored, that is, these interaction probabilities are set to zero. We then proceed with the next largest interaction probability, repeating until all have been acted upon. Note that the diffusive substep size coincides with the total timestep size, so that collisions are assumed to take place instantaneously.

3.3 Coarse-grained Variables

In our simulations, the rods move freely within the domain and with fluctuations in both position and orientation of the rods, it is difficult to identify relatively stable patterns. For this reason, and as an aid for computing divergence and curl, we impose a square grid on the domain with the mesh length d and introduce a coarse-graining procedure to extract observable values, such as the local orientation τ and local density ρ . Using \mathbf{W} to denote the two-dimensional position vector of a grid point (X_i, Y_j) , we calculate the number of rods N whose midpoint positions are in the box $[X_i - d, X_i + d] \times [Y_j - d, Y_j + d]$. The following coarse-grained functions are employed to compute τ and ρ at this grid point (X_i, Y_j) :

$$\begin{aligned}\tau(\mathbf{W}) &= \frac{\sum_{k=1}^N \Phi(|\mathbf{W} - \mathbf{R}_{\mathbf{k}}|) \mathbf{U}_k}{\left| \sum_{k=1}^N \Phi(|\mathbf{W} - \mathbf{R}_{\mathbf{k}}|) \mathbf{U}_k \right|} \\ \rho(\mathbf{W}) &= N\end{aligned}\tag{3.5}$$

Here $|\cdot|$ is Euclidean length and Φ is a weighting function. We take

$$\Phi(s) = e^{-\frac{s^2}{l^2}}\tag{3.6}$$

where l is chosen to be the length of each microtubule. In the simulation we also have to include contributions from “image particles” originating from the periodic boundary conditions.

3.4 Pattern Characterization

We computed the discrete divergence, $\mu = \nabla \cdot \tau$, and the curl, $\omega = \nabla \times \tau$, of the coarse-grained field of the pattern from the last 3000 iterations. Here μ and ω depend

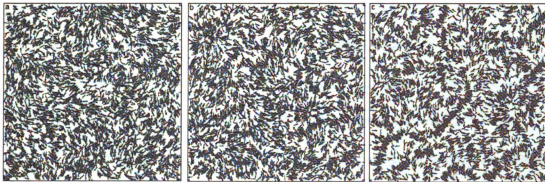


Figure 3.2: Snapshots illustrating the patterns developing in a configuration of 6,000 rods for different motor densities, i.e., different values of P_0 . Arrows represent microtubules, circles depict the cores of vortices or asters. (a) vortices, $t = 620$, $\beta = 1.0$, $P_0 = 0.08$ (low motor density); (b) asters, $t = 602$, $\beta = 0.95$, $P_0 = 0.10$, (high motor density); (c) bundles, $t = 400$, $\beta = 1.0$, $P_0 = 0.15$. See also [100] for movies # 1,2 illustrating the self-organization process.

on the mesh size of the coarse-grained field. By using the central difference scheme, the extrema of μ and ω can be -4 or 4 for an ideal aster or vortex under the 40×40 grid on the 20×20 domain.

The basic idea for pattern characterization is that an aster would have its local divergence greater or less than a threshold value at the center. Similar observations apply to a vortex and its curl. To realize the pattern characterization, we implemented the following procedure:

- Firstly, using the snapshot at $t = 700$, determine the local extrema of μ and ω with values sufficiently far from zero. Specifically:
 1. Compute the minimal value of the divergence μ . Suppose that it occurs at (i, j) ;
 2. Eliminate the surrounding square area consisting of $(2q + 1) \times (2q + 1)$ mesh points. We chose $q = 4$ in our computation, that is, temporarily set $\mu(k, l) = 0$, $i - 4 \leq k \leq i + 4$, $j - 4 \leq l \leq j + 4$. Locate the next minimal value of μ from the remaining region;

3. Repeat step 2 on the remaining region until $\mu > -2.5$;
 4. Use the above three steps to find the maxima of μ with $\mu > 2.5$;
 5. Go through steps 1 to 3 to locate the local minima of ω with $\omega < -2.5$;
 6. Apply a similar procedure to find local maxima of ω with $\omega > 2.5$;
 7. If two of the selected extrema of $|\mu|$ and $|\omega|$ occur in one of the selected squares, then we discard the square that is not centered at a point where the greater of $|\mu|$ and $|\omega|$ occurs.
- Secondly, take the local square area consisting of $(2q+1) \times (2q+1)$ mesh points for each of the extracted locations, and compute four quantities, $\mu_{min}, \mu_{max}, \omega_{min}$ and ω_{max} in this patch for each snapshot from $t = 401$ to $t = 700$.
 - Thirdly, compute the time averages of those four quantities for each patch from these 300 snapshot values, denoted as $\bar{\mu}_{min} = \frac{1}{300} \sum_{i=1}^{300} |\mu_{min}(i)|$, $\bar{\mu}_{max} = \frac{1}{300} \sum_{i=1}^{300} \mu_{max}(i)$, $\bar{\omega}_{min} = \frac{1}{300} \sum_{i=1}^{300} |\omega_{min}(i)|$, and $\bar{\omega}_{max} = \frac{1}{300} \sum_{i=1}^{300} \omega_{max}(i)$. To distinguish between a vortex and an aster, we introduced an additional parameter $\xi = 0.6$, whose use is explained below.
 - Finally, to determine the type of pattern in each local square area, we decide according to the following criteria.
 - If $\bar{\mu}_{min} \geq 3.0$, $\bar{\omega}_{max} < 3.0$, $\bar{\omega}_{min} < 3.0$ and $\bar{\mu}_{max} \leq \xi \bar{\mu}_{min}$, it is an aster.
 - If $\bar{\mu}_{min} \geq 3.0$, $\bar{\omega}_{max} \geq 3.0$ ($\bar{\omega}_{min} \geq 3.0$), $\bar{\omega}_{min} \leq \xi \bar{\mu}_{min}$ ($\bar{\omega}_{max} \leq \xi \bar{\mu}_{min}$) and $\bar{\mu}_{max} \leq \xi \bar{\mu}_{min}$, it is an intermediate form between an aster and a vortex and we assign it an aster-vortex pattern.
 - If $\bar{\mu}_{max} \geq 3.0$, $\bar{\omega}_{max} < 3.0$, $\bar{\omega}_{min} < 3.0$ and $\bar{\mu}_{min} \leq \xi \bar{\mu}_{max}$, the directions of the rods point outwards and it is an anti-aster pattern.

- If $\bar{\mu}_{max} \geq 3.0, \bar{\omega}_{max} \geq 3.0$ ($\bar{\omega}_{min} \geq 3.0$), $\bar{\omega}_{min} \leq \xi \bar{\mu}_{max}$ ($\bar{\omega}_{max} \leq \xi \bar{\mu}_{max}$) and $\bar{\mu}_{min} \leq \xi \bar{\mu}_{max}$, it is an antiaster-vortex pattern.
- If $\bar{\mu}_{min} < 3.0$ and $\bar{\mu}_{max} < 3.0$ and $\bar{\omega}_{min} \geq 3.0$ ($\bar{\omega}_{max} \leq \xi \bar{\omega}_{min}$) or $\bar{\omega}_{max} \geq 3.0$ ($\bar{\omega}_{min} \leq \xi \bar{\omega}_{max}$), then it is a vortex pattern.
- in any other case, it is isotropic.

The parameter space (P_0, β) is in the range $0.01 \leq P_0 \leq 0.15$ and $0.0 \leq \beta \leq 1.0$. We made a grid with stepsizes $\Delta P_0 = 0.01$ and $\Delta \beta = 0.05$ so that we had $15 \times 21 = 315$ mesh points. For each pair of values, we used three different initial conditions for the simulations, using the characterization of the final states described above. We obtained the numbers of asters N_a , aster-vortices N_{av} , antiasters N_{aa} , antiaster-vortices N_{aav} and vortices N_v for each (P_0, β) and we found that $N_{aa} = 0$ and $N_{aav} = 0$. At each parameter grid point we computed two values according to the following formula:

$$M_a(i, j) = \frac{1}{N_1} \sum_{i-1}^{i+1} \sum_{j-1}^{j+1} (N_a + N_{aa}) \quad (3.7)$$

$$M_v(i, j) = \frac{1}{N_1} \sum_{i-1}^{i+1} \sum_{j-1}^{j+1} (N_v) \quad (3.8)$$

For the boundary points, the summations in (3.7) and (3.8) are taken only over the neighboring points around (i, j) within the parameter domain. N_1 in (3.7) and (3.8) is the number of points in the summation. From $M_a(i, j)$ and $M_v(i, j)$, we calculated $\gamma_a(i, j) = \frac{M_a(i, j)}{M_a(i, j) + M_v(i, j)}$ and $\gamma_v(i, j) = \frac{M_v(i, j)}{M_a(i, j) + M_v(i, j)}$. Finally we generated a matrix, I_p , whose entries give the pattern information at that parameter point.

- If $\frac{1}{3}(M_a(i, j) + M_v(i, j)) \leq 1.5$, then it belongs to disordered region and $I_p(i, j) = -1.0$.

- If $\gamma_a(i, j) \geq 0.6$ and $\gamma_v(i, j) \leq 0.4$, then it belongs to aster region and $I_p(i, j) = 1.0$.
- If $\gamma_a(i, j) \leq 0.4$ and $\gamma_v(i, j) \geq 0.6$, then it belongs to vortex region and $I_p(i, j) = 0.0$.
- Otherwise, it belongs to a transition region and $I_p(i, j) = 0.5$.

We used I_p matrix to produce a pseudo-color phase diagram. The pixels with $I_p(i, j) = 1$ are assigned red, the pixels with $I_p(i, j) = 0.5$ yellow, the pixels with $I_p(i, j) = 0.0$ green and the pixels with $I_p(i, j) = -1.0$ blue.

To identify the bundled region, we calculated the density of the rods at each grid point, which is defined as the number of rods whose positions are in the square box with the grid point as the center. Next we computed the global minimal and maximal density in the domain at each time slice. Those minimal and maximal densities were averaged over 300 slices and then over three samples, i.e., $\bar{\rho}_{min} = \frac{1}{3} \sum_1^3 (\frac{1}{300} \sum_{j=1}^{300} \rho_{min}(j))$, $\bar{\rho}_{max} = \frac{1}{3} \sum_1^3 (\frac{1}{300} \sum_{j=1}^{300} \rho_{max}(j))$. If $\bar{\rho}_{min} < 0.2$ and $\bar{\rho}_{max} > 60$, then this point is marked bundled. In the bundled region the rods formed several, with these stripes sometimes forming concentric circles. Moreover asters appear to dominate vortex structures.

3.5 Simulation Results

We applied our model to 6,000 microtubules in a 20×20 domain varying parameters P_0 and β in a wide range with 7,000 time steps in the simulation for each choice of (P_0, β) . It took approximately 69 minutes to complete each run on a SGI Altix 3700 Bx2 with 1.6GHz Itanium2 processors, which is an improvement over the explicit dynamics approach of [81].

We impose a 40×40 grid on the domain to calculate the coarse-grained field.

A snapshot was taken every 10 iterations and so 700 snapshots were obtained for each simulation process. For most of the parameter values chosen, it took about 300 snapshots (3000 time steps) to relax towards relatively stable large scale patterns, and more than 500 snapshots (5000 steps) to become stationary. Some simulations clearly shown a pattern of asters and/or vortices while others resulted in ambiguous patterns. Moreover, the clear-cut distinction between asters and vortices appears to be difficult because of fluctuations. To examine the parameter space (P_0, β) where there are transition regions between asters and vortices, we have devised a pattern characterization scheme. The simulation results obtained from the first four thousand iterations were ignored as they represent transient states. For the last three thousand frames of data, we performed the pattern characterization algorithm given in the last section.

Select simulation results are shown in Figs 3.2, 3.3, 3.4 where $D_{||} = 1/120$ in all simulations. In agreement with the experiments [62, 81] and the theoretical models [2, 3], we obtained an isotropic phase for low motor densities (not shown), and then vortices, transient aster-vortices (structures which resemble vortices near the core and aster far from the core), asters, and bundles with gradual increase of the motor density. Representative snapshots of the rod configurations for three different values of the motor density P_0 are shown in Fig. 3.2 and the two corresponding coarse-grained snapshots of them superimposed with the rod density field are shown in Fig. 3.3. As is evident from our simulation results, a transition from an isotropic (disordered) phase to an oriented phase happens with the increase in the motor density characterized by the parameter P_0 . While due to the small size of the system (only 6,000 particles) we have very strong fluctuations in the number of vortices, asters and anti-asters (structures similar to asters but with the opposite orientation of microtubules; see Fig. 3.4), a general trend can be identified: with the increase in the interaction probability P_0 the average number of vortices decreases while the number of aster increases. For

small values of the anisotropy parameter β asters and anti-asters appears to occur with equal probability. However, with the increase in β the number of anti-asters rapidly decreases while the number of aster increases. For very high motor densities we observed an additional instability resulting in the formation of dense bundles of filaments with the same orientation (see Fig. 3.2c). The bundles are also associated with a certain layering (smectic ordering) of the filaments. This ordering is due to the microscopic interaction law which results in the alignment of the rod midpoints as in Eq. (3.3). While this might be the case for the NCD motors with a large dwelling time, for the kinesin motors the bundles may have a different structure which is not necessarily captured by these simulations. These results are in good agreement with earlier theoretical predictions [2, 3].

The phase diagram delineating various regimes of self-organization is shown in Fig. 3.5. It bears a strong resemblance to the experimental observations [62, 81] and the theoretical model of Refs. [2, 3]. While the boundaries are quite blurred due to strong fluctuations (see Fig. 3.4), there is a transition from vortices to asters with the increase of the interaction rate P_0 . Due to strong fluctuations, pattern characterization is rather difficult, and even sometimes ambiguous. In particular, we often observed anti-aster, i.e. structures with the orientation of rods opposite to that determined by the motion of the motors. Thus, when we calculated the phase diagram, we had to take into account the number of anti-asters and anti-aster-vortices. We also noticed that the rod density in aster regions is greater than that in anti-aster regions. Specifically we found that there were about 80 more rods on average in an aster region than in an anti-aster region. Moreover, the domain of stability of vortices decreases with the increase of the anisotropy parameter β related to the dwell time of the motors, as observed experimentally and in agreement with the continuum model of Refs. [2, 3]. However, we need to emphasize that all the boundaries shown in Fig.3.5 are rather blurred; instead of sharp phase transitions we

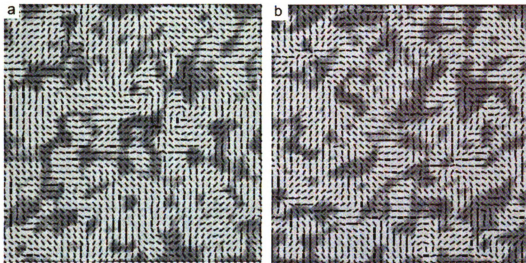


Figure 3.3: Coarse-grained images corresponding to parameters of Fig.3.2 for vortices (a) and asters (b). Arrows represent the orientation field τ . The color (grey levels) shows the density ρ , red (bright) corresponds to the maximum of ρ , and blue (dark) to its minimum. See also [100] for movies # 3,4.

observed only smooth crossovers between different regimes due to strong fluctuations and relatively small number of particles in the system. It is known that in related two-dimensional XY models there is no well-defined second order phase transition from isotropic to ordered phase; the mechanism is related to unbinding of Kosterlitz-Thouless vortices by fluctuations, see [29]. However, sharp phase transition occurs in three dimensions.

The coarse-graining allows for easier identification of aster and vortex structures (see Fig. 3.3). In the movies made using coarse-grained fields we are able to follow the formation, interaction and evolution of asters and vortices. A typical scenario of the dynamical evolution of the system is that small vortices and asters can coalesce to form a larger vortex or aster (see the movies in [100] for parameters $P_0 = 0.12$, $\beta = 1.0$). In accordance with the experiments, vortices have suppression of the microtubule density in the center (holes) and asters lead to an increase of the density

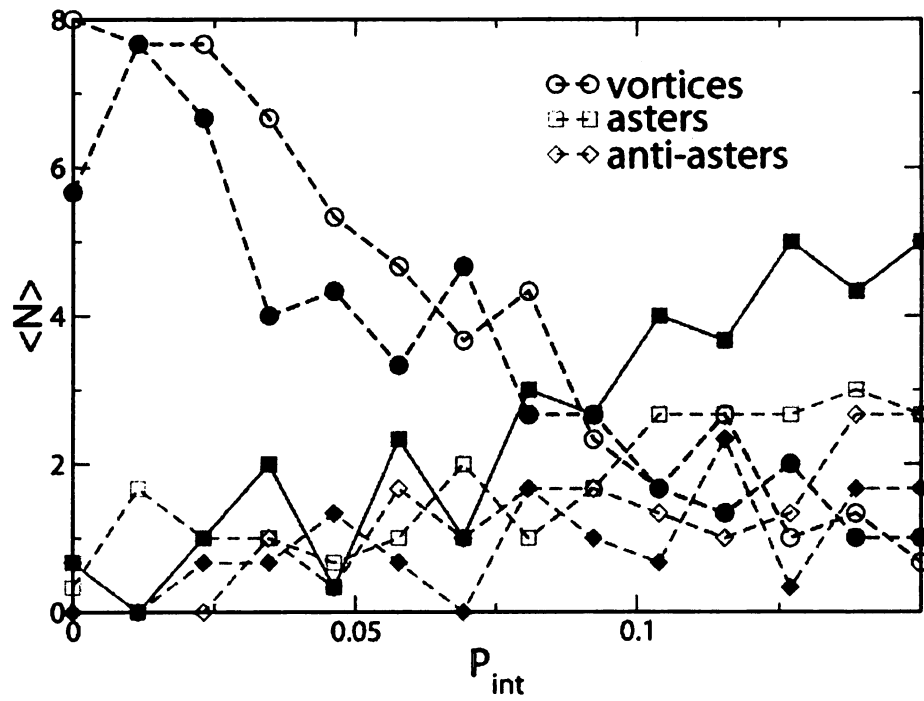


Figure 3.4: Averaged number of asters (squares), anti-asters (diamonds), and vortices (circles) as a function of the interaction probability P_0 for two different values of parameter β . The data for $\beta = 0.35$ is shown in dashed lines, open symbols, and for $\beta = 0.95$ is shown in dotted lines, closed symbols.

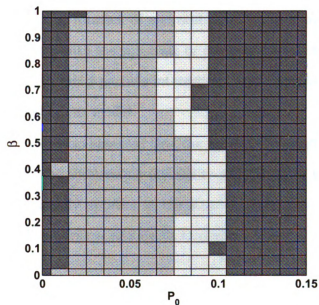


Figure 3.5: Phase diagram of various regimes as a function of the motor density P_0 (the horizontal axis) and the anisotropy parameter β (the vertical axis). The disordered region is blue (black) here; the vortex region is green (grey); the transition from vortex to aster happens at the yellow region (white) and red (dark grey) denotes aster regions. The dashed line denotes the boundary where the rods become bundled.

of microtubules. We have also observed the transformation of vortices into asters in the course of the simulations, likely due to fluctuation and fine size effects.

We followed the trajectory of individual rods in the vicinity of the vortex core in the steady-state. We have found that the particles generally do not rotate around the vortex core. This stems from the fact that in our binary collision algorithm the center of mass of two interacting rods is not displaced in the course of collision, Eq. (3.3). This restriction suppresses directed motion of the rods, and, consequently, global rotation. Thus, the rotation of microtubules seen in experiment [62] is likely related to the interaction with the substrate or the boundary of the container [3, 49], or, possibly is related to multi-particle interactions and anisotropic interaction with the fluid [50] neglected in our model.

In our simulations we also observed that the centers of the asters typically exhibit a drift, reminiscent to the acceleration instability of aster cores predicted in Ref. [3]. This phenomenon especially appears at the stage of formation of asters. However, the precise nature of the drift is still an open question since it could be also due to fluctuation effects.

3.6 Conclusion

A Monte Carlo type stochastic approach has been developed to conduct the study of self-organization of microtubules mediated by molecular motors. The approach allows us to bypass the fast time scales associated with the diffusion and the motion of individual molecular motors and concentrates on the relevant features of the long-time and large-scale behaviors associated with the self-organization phenomena.

While a direct comparison with the earlier algorithms introduced in Ref. [63] is not always possible due to the different nature of the approximations, some rough estimates are useful. The total simulation time reported in Ref [63] was 1500 sec.

The characteristic time scale of the simulations of the order of 1 sec can be inferred from the density of microtubules (about $0.05 \mu m^{-2}$, or about 500 microtubules in a box 100×100 microns) and the motor diffusion ($D = 20 \mu m^2/s$), which roughly corresponds to 10^3 dimensionless units of time. Our simulations, performed with much higher number of microtubules (6000) and in bigger boxes were performed for about 1000 dimensionless time units, that is, about the same order of magnitude as in Refs. [62, 63].

Our method can be easily adapted to new experimental settings, such as a motor and microtubule system with a fraction of the motors permanently bound to the substrate [49]. Our results are complimentary to the analytical studies of self-organization in the framework of amplitude equations derived from the stochastic master equations, and provide valuable tests for a variety of phenomenological continuum theories of cytoskeleton formation [51, 55, 50, 92]. Moreover, our simulations shed a new light on the microscopic details of self-organization not available in the continuum formulation. We anticipate that somewhat similar approaches can be applied to a broad range of systems, such as networks of actin filaments interacting with myosin motors [35], patterns emerging in granular systems with anisotropic particles [10, 48, 6, 60, 5], and systems of self-propelled objects [99, 28].

Chapter 4

Summary and Future work

In the first part of the thesis, we have developed a set of algorithms which tightly follow the mechanochemical transition process of kinesin motors. The mechanical moving process is described by a 3D Langevin equation, solved numerically by the Euler scheme of stochastic differential equations. The chemical reaction process is simulated by a Monte Carlo method. These two processes are coupled in the simulation by following the consensus walking model of kinesin so far obtained by biologists (See [11] and reference therein). We carried out a detailed simulation of the walking of the wild type and its mutants with extended neck-linkers and obtained results in line with the experimental results [95]. In this process, we discussed different approaches for the estimate of the tension in the neck-linkers by using models from polymer science. We explored the binding mechanism by working out and testing different binding probability formulas for the tethered head. In our analysis of the processivity of kinesin, we also clarified the role of the front-gated-head and the rear-gated-head hypotheses in the regulation of the processivity. Our conclusion is that both of them should work together.

Based on the algorithm developed, we can further take into account the backward walking of the kinesin which is not included in our model because the probability of

backward stepping is small. Furthermore, it is interesting to derive an overdamped beam equation to describe the swing process of the tethered head triggered by the neck-linker docking. For those mutants with longer neck-linkers, the potential stored in the neck-linkers is small and thus it takes more time for the tethered head to be swung to a forward binding site.

In the second part of the thesis, motivated by the experiment [62] and the theoretical work [2, 3], we performed Monte Carlo simulations of a large system (including 6000 thousand microtubules) in a large parameter space while the numerical simulation in [2, 3] was carried out in a small neighborhood of parameter space. We devised an algorithm to select binary collisions in the cases of multiple intersections. We also developed a procedure to characterize the patterns. Our results have reproduced the consecutive transitions from the disordered state to the vortex state, to the aster state, and then to the bundled state when the motor concentration increases. This phase transition is in agreement with the experimental results [62], while the other models [51, 78] failed to reproduce these experimental results.

Appendix A

Pseudo Code of the Algorithms

First, we introduce some indexes used in the pseudo codes.

- $H1_{bw}$ is the index of head1 backward binding. 1=the bound state, 0=the unbound state. $H1_{bw} = 1$ when the kinesin begins a new step.
- $H1_{fw}$ is the index of head1 forward binding. 1=the bound state, 0=the unbound state. The default value of $H1_{fw}$ is 0. It will be 1 when head1 binds to a forward site.
- $H2_{st}$ is a 1×5 index matrix. The first column is for bound state, 1=the bound state 0=the unbound state; the second is for ATP bound state, 0=the ATP empty state, 1= the ATP bound st; the third column is for neck-linker zipping, 0=the unzipped state, 1=the unzipped state; the fourth column is for ATP hydrolysis, 0=ATP not hydrolyzed, 1= ATP hydrolyzed; the fifth column is for P_i release, 0= P_i not released, 1= P_i released and head2 is in microtubule bound with the ADP in the catalytic core. $H2_{st} = [1, 0, 0, 0, 0]$ when the kinesin begins a new step.

Algorithm 1 This is the part one of the whole algorithm.

$H1_{bw} = 1$, $H1_{fw} = 0$, and $H2_{st}(1, 1) = 1$

while $H1_{fw} = 0$ and $H2_{st}(1, 1) = 1$ **do**

while $H1_{bw} = 1$ **do**

 Compute the tension in the neck-linkers by (2.9)

$$k_{dMT} = k_{dMT}^0 e^{\frac{F\delta_C^1}{K_B T}}$$

$$k_{zip} = k_{zip}^0 e^{-\frac{F\delta_C^3}{K_B T}}$$

if $H2_{st}(1, 3) = 0$ **then**

if $\zeta \leq k_{dMT} dt$ **then**

$H1_{bw} = 0$

end if

if $H2_{st}(1, 2) = 1$ **then**

if $\zeta \leq k_{dATP}^- dt$ **then**

$H2_{st}(1, 2) = 0$

else if $k_{dATP}^- dt < \zeta \leq (k_{dATP}^- + k_{zip}) dt$ **then**

 The neck-linker is docked. For the wild type. this docking induce the dissociation of head1 from the microtubule, i.e., $H1_{bw} = 0$, because of the restriction of the neck-linkers. For the mutants, this docking may not trigger the detachment of head1 from microtubule.

end if

else

if $\zeta \leq k_{dATP}^+ dt$ **then**

$H2_{st}(1, 2) = 1$

end if

end if

end if

if $H2_{st}(1, 3) = 1$ **then**

if $\zeta \leq k_{dMT} dt$ **then**

$H1_{bw} = 0$

end if

 Consider the ATP hydrolysis in head2

end if

end while

end while

Algorithm 2 This is the part two of the whole algorithm, following the part 2

```

while  $H1_{fw} = 0$  and  $H2_{st}(1, 1) = 1$  do
  if  $H2_{st}(1, 3) = 0$  then
    if  $H2_{st}(1, 2) = 1$  then
      if  $\zeta \leq k_{dATP}^- dt$  then
         $H2_{st}(1, 2) = 0$ 
      else if  $k_{dATP}^- dt < \zeta \leq (k_{dATP}^- + k_{zip}^0) dt$  then
        The neck-linker is docked.
      end if
    else
      if  $\zeta \leq k_{dATP}^+ dt$  then
         $H2_{st}(1, 2) = 1$ 
      end if
    end if
    Compute the tension in the neck-linkers by (2.9) and (2.12).
    Update the position of head1 according to (2.20).
  end if
  if  $H2_{st}(1, 3) = 1$  then
    Compute the tension in the neck-linkers by (2.9) and (2.12).
    Update the position of head1 according to (2.20).
    Consider the ATP hydrolysis in head2
  end if
  if the distance between head1 and a binding site is less than 2.5 nm then
    Consider the possibility of the binding to that site by using the formula (2.23)
    if head1 binds to a backward binding site then
       $H1_{bw} = 1$ 
    end if
    if head1 binds to a forward binding site then
       $H1_{fw} = 1$ 
    end if
  end if
end while
Consider the ADP release in head1. Head1 does not bind an ATP molecule until
the  $P_i$  is released in head2. When head1 is in the empty state and head2 is in the
ADP bound state, a complete chemomechanical cycle is finished.

```

BIBLIOGRAPHY

- [1] Alonso, M.C., Drummond, D.R., Kain, S., Hoeng, J., Amos, L. and Cross, R.A., (2007). An ATP gate controls tubulin binding by the tethered head of kinesin-1. Science. 316: 120–123.
- [2] Aranson, I.S. and Tsimring, L.S., (2005). Pattern formation of microtubules and motors: Inelastic interaction of polar rods. Physical Review E. 74: 050901.
- [3] Aranson, I.S. and Tsimring, L.S., (2006). Theory of self-assembly of microtubules and motors. Physical Review E. 74: 031915.
- [4] Aranson, I.S. and Tsimring, L.S., (2006). Patterns and collective behavior in granular media: Theoretical concepts. Review of Modern Physics. 78: 641.
- [5] Aranson, I.S., Volfson, D., and Tsimring, L.S., (2007). Swirling motion in a system of vibrated elongated particles. Physical Review E. 75: 051301.
- [6] Aranson, I.S. and Tsimring, L.S., (2003). Model of coarsening and vortex formation in vibrated granular rods. Physical Review E. 67: 021305.
- [7] Asenjo, A.B. and Sosa, H., (2009). A mobile kinesin-head intermediate during the ATP-waiting state. Proc. Natl. Acad. Sci.. 106: 5657-5662.
- [8] Asbury, C.L., Fehr, A.N. and Block, S.M., (2003). Kinesin moves by an asymmetric hand-over-hand mechanism. Science. 302: 2130-2134.
- [9] Blanchet, A., Dolbeault, J., and Kowalczyk, M., (2009). Stochastic Stokes' drift, homogenized functional inequalities, and large time behavior of Brownian ratchets. SIAM J. Math. Anal.. 41: 46–76.
- [10] Blair, D. L., Neicu, T., and Kudrolli, A., (2003). Vortices in vibrated granular rods. Physical Review E. 67: 031303.
- [11] Block, S. M., (2007). Kinesin motor mechanics: binding, stepping, tracking, gating, and limping. Biophys J.. 92: 2986–2995.

- [12] Budhiraja, A. and Fricks, J., (2006). Molecular motors, brownian ratchets, and reflected diffusions. Discrete and Continuous Dynamical Systems. 6: 711–734.
- [13] Carter, N. J. and Cross, R. A., (2005). Mechanics of the kinesin step. Nature. 435: 308–312.
- [14] Chakravarty, A., Howard, L., and Compton, D.A., (2004). A mechanistic model for the organization of microtubule asters by motor and non-motor proteins in a mammalian mitotic extract. Molecular biology of the cell. 15: 2116–2132.
- [15] Chipot, M., Hastings, S., and Kinderlehrer, D., (2004). Transport in a molecular motor system. M2AN Math. Model. Numer. Anal.. 38: 1011–1034.
- [16] Chipot, M., Hilhorst, D., Kinderlehrer, D., and Olech, M., (2009). Contraction in L^1 for a system arising in chemical reactions and molecular motors. Differ. Equ. Appl.. 1: 139–151.
- [17] Coy, D. L., Wagenbach, M., and Howard, J., (1999). Kinesin takes one 8-nm step for each ATP that it hydrolyzes J. Biol. Chem.. 274: 3667–3671.
- [18] Cross, R. A., (2004). The kinetic mechanism of kinesin. Trends Biochem. Sci.. 29: 301–309.
- [19] Cytrynbaum, E.N., Rodionov, V., and Mogilner, A., (2004). Computational model of dynein-dependent self-organization of microtubule asters. J. Cell Sci.. 117: 1381–1397.
- [20] de Gennes, P.-G. and Prost, J., (1995). The Physics of Liquid Crystals. Clarendon Press, Oxford.
- [21] Derrida, B., (1983). Velocity and diffusion constant of a periodic one-dimensional hopping model. J. Stat. Phys.. 31: 433–450.
- [22] Doi, M. and Edwards, S.F. (1988). The Theory of Polymer Dynamics. Clarendon Press, Oxford.
- [23] Fisher, M.E. and Kolomeisky, A.B., (1999). The force exerted by a molecular motor. Proc. Natl. Acad. Sci.. 96: 6597–602.
- [24] Fisher, M.E. and Kolomeisky, A.B., (1999). Molecular motors and the forces they exert. Physica A. 274: 241–266.
- [25] Fisher, M.E. and Kolomeisky, A.B., (2001). Simple mechanochemistry describes the dynamics of kinesin molecules. Proc. Natl Acad. Sci.. 98: 7748–7753.
- [26] Gennerich, A., Carter, A.P., Reck-Peterson, S.L., and Vale, R.D., (2007). Force-induced bidirectional stepping of cytoplasmic Dynein. Cell. 131: 952–965.

- [27] Gennerich, A. and Vale, R.D. (2009). Walking the walk: How kinesin and dynein coordinate their steps. Current Opinion in Cell Biology. 21: 59–67.
- [28] Grégoire, G. and Chaté, H., (2004). Onset of collective and cohesive motion. Physical Review Letter. 92: 025702.
- [29] Gupta, R., DeLapp, J., Batrouni, G.G., Fox, G.C., Baillie, C.F., and Apostolakis, J., (1988). Physical Review Letter. 61: 1996.
- [30] Guydosh, N.R. and Block, S.M., (2006). Backsteps induced by nucleotide analogs suggest the front head of kinesin is gated by strain. Proc. Natl. Acad. Sci. 103: 8054-8059.
- [31] Hancock, W.O. and Howard, J., (1999). Kinesins processivity results from mechanical and chemical coordination between the ATP hydrolysis cycles of the two motor domains. PNAS. 96: 13147-13152.
- [32] Howard, J., (2000). Mechanics of Motor Proteins and the Cytoskeleton. Springer, New York, 2000.
- [33] Howard J., (1996). The movement of kinesin along microtubules. Annu. Rev. Physiol. 58: 703–729.
- [34] Hua, W., Young, E.C., Fleming, M.L., and Gelles, J. (1997). Coupling of kinesin steps to ATP hydrolysis. Nature. 388: 390-393
- [35] Humphrey, D., Duggan, C., Saha, D., Smith, D. and Käs, J., (2002). Active fluidization of polymer networks through molecular motors. Nature. 416: 413–16.
- [36] Hyeon, C. and Onuchic, J.N., (2007). Internal strain regulates the nucleotide binding site of the kinesin leading head Pro. Natl. Acad. Sci. 104: 2175-2180.
- [37] Hyman, A.A. and Karsenti, E., (1996). Morphogenetic properties of microtubules and mitotic spindle assembly Cell. 84: 401-410.
- [38] Jamali, Y., Lohrasebi, H. and Rafii-Tabar, H., (2007). Computational modeling of the stochastic dynamics of kinesin biomolecular motors. Physica A. 381: 239–254.
- [39] Jia, Z., Karpeev, D., Aranson, I., and Bates, P., (2008). Simulation studies of self-organization of microtubules and molecular motors. Physical Review E. 77: 051905.
- [40] Julicher, F., Ajdari, A., and Prost, J., (1997). Modeling molecular motors. Rev. Mod. Phys. 69: 1269-81.
- [41] van Kampen N.G., (1981). Stochastic Processes in Physics and Chemistry. North-Holland Publishing Company.

- [42] Kanada, R. and Sasaki, K., (2003). Theoretical model for motility and processivity of two-headed molecular motors. Phys. Rev. E. 67: 061917.
- [43] Karpeev, D., Aranson, I., Tsimring, L., and Kaper, H., (2007). Interactions of semiflexible filaments and molecular motors. Physical Review E. 76: 051905.
- [44] Keller, D. and Bustamante, C., (2000). The mechanochemistry of molecular motors. Biophysical Journal. 78: 541–556.
- [45] Kikkawa, M., (2008). The role of microtubules in processive kinesin movement. Trends in Cell Biology. 18: 128–135.
- [46] Kinderlehrer, D. and Kowalczyk, M., (2002). Diffusion-mediated transport and the flashing ratchet. Arch. Ration. Mech. Anal. 161. no. 2: 149–179.
- [47] Kolomeisky, A. and Fisher, M., (2007). Molecular motors: A theorist's perspective. Annu. Rev. Phys. Chem. 58: 675–95.
- [48] Kudrolli, A., Lumay, G., Volfson, D., and Tsimring, L. S., (2008). Swarming and swirling in self-propelled polar granular rods. Physical Review Letter. 100: 058001.
- [49] Kraikivski, P., Lipowsky, R., and Kierfeld, J., (2006). Enhanced ordering of interacting filaments by molecular motors. Physical Review Letter. 96: 258103.
- [50] Kruse, K., Joanny, J.F., Julicher, F., Prost, J., and Sekimoto, K., (2004). Asters, vortices, and rotating spirals in active gels of polar filaments. Physical Review Letter. 92: 078101.
- [51] Lee, H.Y. and Kardar, M., (2001). Macroscopic equations for pattern formation in mixtures of microtubules and molecular motors. Phys. Rev. E. 64: 056113.
- [52] Leibler S and Huse, D.A., (1993). Porters versus rowers: a unified stochastic model of motor proteins. J. Cell Biol. 121:1356-68.
- [53] Levine, A. J., Liverpool, T. B., and MacKintosh, F. C., (2004). Phys. Rev. E. 69: 021503.
- [54] Liepelt, S. and Lipowsky, R., (2007). Kinesin's network of chemomechanical motor cycles. Phys. Rev. Lett. 98: 258102.
- [55] Liverpool, T.B. and Marchetti, M.C., (2003). Instabilities of Isotropic Solutions of Active Polar Filaments. Phys. Rev. Lett. 90: 138102.
- [56] Mori, T., Vale, R.D., and Tomishige, M., (2007). How kinesin waits between steps. Nature. 450: 750-754.
- [57] Munarriz, J., Mazo, J.J., and Falo, F., (2008). Model for hand-over-hand motion of molecular motors. Phys. Rev. E. 77: 031915.

- [58] Mather, W.H. and Fox, R.F., (2006). Kinesin's Biased Stepping Mechanism: Amplification of neck-linker Zippering. Biophys J. 91: 2416–2426.
- [59] Mogilner, A, Fisher, A.J. and Baskin, R.J., (2001). Structural changes in the neck-linker of kinesin explain the load dependence of the motor's mechanical cycle. J. Theor. Biol. 211: 143-57.
- [60] Narayan, V., Menon, N., and Ramaswami, S., (2006). Nonequilibrium steady states in a vibrated-rod monolayer: tetratic, nematic, and smectic correlations. J. Stat. Mech. P01005.
- [61] Nédélec, F.J., (2002). Computer simulations reveal motor properties generating stable antiparallel microtubule interactions. J. Cell Biology. 158: 1005-1015.
- [62] Nédélec, F.J., Surrey, T., Maggs, A.C., and Leibler, S., (1997). Self-organization of microtubules and motors, Nature. 389: 305–308.
- [63] Nédélec, F., Surrey, T., and Maggs, A.C., (2001). Dynamic concentration of motors in microtubule arrays. Physical Review Letter. 86: 3192.
- [64] Nicholas, F.E., Yoshioka, C., Milligan A.R., and Vale, D.R., (2006). A lever-arm rotation drives motility of the minus-end-directed kinesin Ncd. Nature. 439: 875–878.
- [65] Parmeggiani, A., Julicher, F., Ajdari, A. and Prost, J., (1999). Energy transduction of isothermal ratchet: Generic aspects and specific examples close to and far from equilibrium. Phys. Rev. E. 60: 2127-2140.
- [66] Perthame, B. and Souganidis, P.E., (2009). Asymmetric potentials and motor effect: a large deviation approach. Arch. Ration. Mech. Anal. 193: 153–169.
- [67] Perthame, B., (2007). Transport Equations in Biology. Frontiers in Mathematics. Birkhauser, Boston.
- [68] Peskin, C.S. and Oster, G. (1995). Coordinated hydrolysis explains the mechanical behavior of kinesin. Biophys. J. 68: S202-11.
- [69] Phillips, R., Kondev, J., and Theriot, J. (2009). Physical Biology of the Cell. Taylor & Francisc Group.
- [70] Qian, H., (1997). A simple theory of motor protein kinetics and energetics. Biophysical chemistry. 67: 263–267.
- [71] Qian, H., (2000). A simple theory of motor protein kinetics and energetics. II. Biophysical chemistry. 83: 35–43
- [72] Reck-Peterson, S.L., Yildiz, A., Carter, A.P., Gennerich, A., Zhang, N., and Vale, R.D., (2006). Single molecule analysis of dynein processivity and stepping behavior. Cell. 126: 335–348.

- [73] Reimann, P., (2002). Brownian motors: noisy transport far from equilibrium. Phys. Rep. 361: 57-265
- [74] Rice, S., Lin, A.W., Safer, D.C., Hart, L., Naber, N., Carragher, B.O., Cain, S.M., Pechatnikova, E., Wilson-Kubalek, E.M., Whittaker, M., Pate, E., Cooke, R., Taylor, E.W., Milligan, A.R., and Vale, R.D., (1999). A structural change in the kinesin motor protein that drives motility. Nature. 402: 778-784.
- [75] Rice, S., Cui, Y., Sindelar, C., Naber, N., Matuska, M., Vale R., and Cooke, R., (2003). Thermodynamic properties of the kinesin neck-region docking to the catalytic core. Biophys. J. 84: 1844-1854.
- [76] Rosenfeld, S.S., Jefferson, G.M. and King, P.H., (2001). ATP reorients the neck-linker of kinesin in two sequential steps. J. Biol. Chem. 276: 40167-40174.
- [77] Rosenfeld, S.S., Fordyce, P.M., Jefferson, G.M., King, P.H., and Block, S.M., (2003). Stepping and stretching: how kinesin uses internal strain to walk processively. J. Biol. Chem. 278: 18550-18556.
- [78] Sankararamn, S., Menon, G.I., and Sunial Kumar, P.B., (2004). Self-organized pattern formation in motor-microtubule mixtures. Physical Review E. 70: 031905.
- [79] Schliwa, M. and Woehike, G., (2003). Molecular motors. Nature. 422: 759-765.
- [80] Sindelar, C.V. and Downing, K.H., (2007). The beginning of kinesin's force-generating cycle visualized at 9-A resolution. J. Cell Biology. 177: 377-385.
- [81] Surrey, T., Nédélec, F., Leibler, S., and Karsenti, E. (2001). Physical properties determining self-organization of motors and microtubules. Science. 292: 1167-1171.
- [82] Svoboda, K. and Block, S.M., (1994). Force and velocity measured for single kinesin molecules. Cell. 77: 773-784.
- [83] Schnitzer, M.J., Visscher, K. and Block, S.M., (2000). Force production by single kinesin motors. Nature cell biology. 2: 718-723.
- [84] Schnitzer, M.J. and Block, S.M., (1997). Kinesin hydrolyses one ATP per 8-nm step, Nature. 388: 386-390.
- [85] Schief, W.R., Clark, R.H., Crevenna, A.H., and Howard, J., (2004). Inhibition of kinesin motility by ADP and phosphate supports a hand-over-hand mechanism. PNAS. 101: 1183-1188.
- [86] Takiguchi, K., (1991). Heavy-meromyosin induces sliding movements between antiparallel actin filaments. J. Biochem. (Tokyo). 109: 250.

- [87] Taniguchi, Y., Nishiyama, M., Ishii, Y., and Yanagida, T., (2005). Entropy rectifies the Brownian steps of kinesin. Nat Chem Biol. 1: 342-347.
- [88] Tsygankov, D., Linden, M., and Fisher, M.E., (2007). Back-stepping, hidden substeps, and conditional dwell times in molecular motors. Physical Review E. 75: 021909.
- [89] Uemura, S., kawaguchi, K., Yajima, J., Edamatsu, M., Toyoshima, Y.Y., and Ishiwata, S., (2002). Kinesin-microtubule binding depends on both nucleotide state and loading direction. Proc. Natl. Acad. Sci. 99: 5977-5981.
- [90] Urrutia, R., McNiven, M.A., Albanesi, J.P., Murphy, D.B., and Kachar, B., (1991). Purified kinesin promotes vesicle motility and induces active sliding between microtubules in vitro. Proc. Natl. Acad. Sci. 88: 6701.
- [91] Valentine, M.T. and Gilbert, S.P., (2007). To step or not to step? How biochemistry and mechanics influence processivity in Kinesin and Eg5. Curr. Opin. in Cell Bio. 19: 75-81.
- [92] Voituriez, R., Joanny, J.F., and Prost, J., (2006). Generic phase diagram of active polar films. Physical Review Letter. 96: 028102.
- [93] Yildiz, A., Tomishige, M., Vale, R.D., and Selvin, P.R., (2004). Kinesin walks hand-over-hand. Science. 303: 676-679.
- [94] Yildiz, A. and Selvin, P.R., (2005). Kinesin: walking, crawling or sliding along. Trends in cell biology. 15: 112-120.
- [95] Yildiz, A., Tomishige, M., Gennerich, A., and Vale, R.D., (2008). Intramolecular strain coordinates kinesin stepping behavior along microtubules. Cell. 134: 1030-1041.
- [96] Ziebert, F. and Zimmermann, W., (2005). Nonlinear competition between asters and stripes in filament-motor systems. Eur. Phys. J. E. 18: 41.
- [97] Ziebert, F., Aranson, I.S., and Tsimring, L.S., (2007). Effects of cross-links on motor-mediated filament organization. New Journal of Physics. 9: 421.
- [98] Hahlen, K., Ebbing, B., Reinders, J., Mergler, J., Sickmann, A., and Woehlke, G., (2006). Feedback of the Kinesin-1 neck-linker Position on the Catalytic Site, J. Biol. Chem. Vol: 281, no: 27: 18868-18877.
- [99] Vicsek, T., Czirók, A., Ben-Jacob, E., Cohen, I., and Shochet, O., (1995). Novel type of phase-transition in a system of self-driven particles. Physical Review Letter. 75: 1226.

[100] See EPAPS Document No. E-PLEEE8-77-016805 for computer animations of simulations results. A direct link to this document may be found in the online article's HTML reference section. The document may also be reached via the EPAPS homepage (<http://www.aip.org/pubservs/epaps.html>) or from <ftp.aip.org> in the directory /epaps/. See the EPAPS homepage for more information.

MICHIGAN STATE UNIVERSITY LIBRARIES



3 1293 03063 0267